Fermi National Accelerator Laboratory

FERMILAB-Pub-90/137 -E
[E-741/CDF]

Top Quark Search in the Electron + Jets Channel in Proton-Antiproton Collisions at $\sqrt{s}$ = 1.8 TeV*

F. Abe[8], D. Amidei[4], G. Apollinari[11], M. Atac[4], P. Auchincloss[14], A. R. Baden[6], A. Bamberger[19], A. Barbaro-Galtieri[9], V. E. Barnes[12], F. Bedeschi[11], S. Behrends[12], S. Belforte[11], G. Bellettini[11], J. Bellinger[18], J. Bensinger[2], A. Beretvas[4], J. P. Berge[4], S. Bertolucci[5], S. Bhadra[7], M. Binkley[4], R. Blair[1], C. Blocker[2], A. W. Booth[4], G. Brandenburg[6], D. Brown[6], E. Buckley[14], A. Byon[12], K. L. Byrum[18], C. Campagnari[3], M. Campbell[3], R. Carey[6], W. Carithers[9],D. Carlsmith[18], J. T. Carroll[4],R. Cashmore[19], F. Cervelli[11], K. Chadwick[4], G. Chiarelli[5], W. Chinowsky[9], S. Cihangir[4], A. G. Clark[4], D. Connor[10], M. Contreras[2], J. Cooper[4], M. Cordelli[5], D. Crane[4], M. Curatolo[5], C. Day[4], S. Dell'Agnello[11], M. Dell'Orso[11], L. DeMortier[2], P. F. Derwent[3], T. Devlin[14], D. DiBitonto[15], R. B. Drucker[9], J. E. Elias[4], R. Ely[9], S. Errede[7], B. Esposito[5], B. Flaugher[14], G. W. Foster[4], M. Franklin[6], J. Freeman[4], H. Frisch[3], Y. Fukui[8],Y. Funayama[16], A. F. Garfinkel[12], A. Gauthier[7],S. Geer[6], P. Giannetti[11], N. Giokaris[13], P. Giromini[5], L. Gladney[10], M. Gold[9], K. Goulianos[13], H. Grassman[11], C. Grosso-Pilcher[3], C. Haber[9], S. R. Hahn[4], R. Handler[18], K. Hara[16], R. M. Harris[9], J. Hauser[3], T. Hessing[15], R. Hollebeek[10], L. Holloway[7], P. Hu[14], B. Hubbard[9], B. T. Huffman[12], R. Hughes[10], P. Hurst[7], J. Huth[4], M. Incagli[11], T. Ino[16], H. Iso[16], H. Jensen[4], C. P. Jessop[6], R. P. Johnson[4], U. Joshi[4], R. W. Kadel[4], T. Kamon[15], S. Kanda[16], D. A. Kardelis[7] I. Karliner[7], E. Kearns[6], R. Kephart[4], P. Kesten[2], R. M. Keup[7], H. Keutelian[7], S. Kim[16], L. Kirsch[2], K. Kondo[16], S. E. Kuhlmann[1], E. Kuns[14], A. T. Laasanen[12], J. I. Lamoureux[18], W. Li[1], T. Liss[3], N. Lockyer[10], C. B. Luchini[7], P. Maas[4], M. Mangano[11], J. P. Marriner[4], R. Markeloff[18], L. A. Markosky[17], R. Mattingly[2], P. McIntyre[15], A. Menzione[11], T. Meyer[15], S. Mikamo[8], M. Miller[3], T. Mimashi[16], S. Miscetti[5], M. Mishina[8],S. Miyashita[16], Y. Morita[16], S. Moulding[2], A. Mukherjee[4], Y. Muraki[16], L. Nakae[2], I. Nakano[16], C. Nelson[4], C. Newman-Holmes[4], J. S. T. Ng[6], M. Ninomiya[16], L. Nodulman[1], S. Ogawa[16], R. Paoletti[11], A. Para[4], E. Pare[6], J. Patrick[4], T. J. Phillips[6], R. Plunkett[4], L. Pondrom[18], J. Proudfoot[1], G. Punzi[11], D. Quarrie[4], K. Ragan[10], C. Redlinger[3], J. Rhoades[18], F. Rimondi[19], L. Ristori[11], T. Rohaly[10], A. Roodman[3], A. Sansoni[5], R. D. Sard[7], A. Savoy-Navarro[19], V. Scarpine[7], P. Schlabach[7], E. E. Schmidt[4], M. H. Schub[12], R. Schwitters[6], A. Scribano[11], S. Segler[4], Y. Seiya[16], M. Sekiguchi[16], P. Sestini[11], M. Shapiro[6], M. Sheaff[18], M. Shochet[3], J. Siegrist[9], P. Sinervo[10], J. Skarha[18], K. Sliwa[17], D. A. Smith[11], F. D. Snider[3], R. St. Denis[6], A. Stefanini[11], R. L. Swartz, Jr.[7], M. Takano[16], K. Takikawa[16], S. Tarem[2], D. Theriot[4],M. Timko[15], P. Tipton[9], S. Tkaczyk[4], A. Tollestrup[4], G. Tonelli[11], J. Tonnison[12], W. Trischuk[16] Y. Tsay[3], F. Ukegawa[16], D. Underwood[1], R. Vidal[4], R. G. Wagner[1], R. L. Wagner[4], J. Walsh[10], T. Watts[14], R. Webb[15], C. Wendt[18], W. C. Wester, III[9], T. Westhusing[11], S. White[13], A. Wicklund[1], H. H. Williams[10], B. Winer[9], A. Yagil[4],A. Yamashita[16], K. Yasuoka[16], G. P. Yeh[4], J. Yoh[4], M. Yokoyama[16], J. C. Yun[4], F. Zetti[11],

[1] Argonne National Laboratory, Argonne, Illinois 60439 - [2] Brandeis University, Waltham, Massachusetts 02254 - [3] University of Chicago, Chicago, Illinois 60637 - [4] Fermi National Accelerator Laboratory, Batavia, Illinois 60510 - [5] Laboratori Nazionali di Frascati, Instituto Nazionale di Fiscia Nucleare, I-00044, Frascati, Italy - [6] Harvard University, Cambridge, Massachusetts 02138 - [7] University of Illinois, Urbana, Illinois 61801 - [8] National Laboratory for High Energy Physics (KEK), Tsukuba-gun, Ibaraki-ken 305, Japan - [9] Lawrence Berkeley Laboratory, Berkeley, California 94720 - 10 University of Pennsylvania, Philadelphia, Pennsylvania 19104 - [11] INFN, University and Scuola Normale Superiore of Pisa, I-56100 Pisa, Italy - [12] Purdue University, West Lafayette, Indiana 47907 - [13] Rockefeller University, New York, New York 10021 - [14] Rutgers University, Piscataway, New Jersey 08854 - [15] Texas A&M University, College Station, Texas 77843 - [16] University of Tsukuba, Tsukuba, Ibaraki 305, Japan - [17] Tufts University, Medford, Massachusetts 02155- [18] University of Wisconsin, Madison, Wisconsin 53706 - [19] Visitor

July 11, 1990

* Submitted to Phys. Rev. D..

FERMILAB-PUB-90/137-E

UPR-0193E

July 11, 1990

Top Quark Search in the Electron + Jets Channel in Proton-Antiproton Collisions at $\sqrt{s} = 1.8$ TeV

F. Abe,[8] D. Amidei,[4] G. Apollinari,[11] M. Atac,[4] P. Auchincloss,[14] A. R. Baden,[6] A. Bamberger,[19] A. Barbaro-Galtieri,[9] V. E. Barnes,[12] F. Bedeschi,[11] S. Behrends,[12] S. Belforte,[11] G. Bellettini,[11] J. Bellinger,[18] J. Bensinger,[2] A. Beretvas,[4] J. P. Berge,[4] S. Bertolucci,[5] S. Bhadra,[7] M. Binkley,[4] R. Blair,[1] C. Blocker,[2] A. W. Booth,[4] G. Brandenburg,[6] D. Brown,[6] E. Buckley,[14] A. Byon,[12] K. L. Byrum,[18] C. Campagnari,[3] M. Campbell,[3] R. Carey,[6] W. Carithers,[9] D. Carlsmith,[18] J. T. Carroll,[4] R. Cashmore,[19] F. Cervelli,[11] K. Chadwick,[4] G. Chiarelli,[5] W. Chinowsky,[9] S. Cihangir,[4] A. G. Clark,[4] D. Connor,[10] M. Contreras,[2] J. Cooper,[4] M. Cordelli,[5] D. Crane,[4] M. Curatolo,[5] C. Day,[4] S. Dell'Agnello,[11] M. Dell'Orso,[11] L. DeMortier,[2] P. F. Derwent,[3] T. Devlin,[14] D. DiBitonto,[15] R. B. Drucker,[9] J. E. Elias,[4] R. Ely,[9] S. Errede,[7] B. Esposito,[5] B. Flaugher,[14] G. W. Foster,[4] M. Franklin,[6] J. Freeman,[4] H. Frisch,[3] Y. Fukui,[8] Y. Funayama,[16] A. F. Garfinkel,[12] A. Gauthier,[7] S. Geer,[6] P. Giannetti,[11] N. Giokaris,[13] P. Giromini,[5] L. Gladney,[10] M. Gold,[9] K. Goulianos,[13] H. Grassmann,[11] C. Grosso-Pilcher,[3] C. Haber,[9] S. R. Hahn,[4] R. Handler,[18] K. Hara,[16] R. M. Harris,[9] J. Hauser,[3] T. Hessing,[15] R. Hollebeek,[10] L. Holloway,[7] P. Hu,[14] B. Hubbard,[9] B. T. Huffman,[12] R. Hughes,[10] P. Hurst,[7] J. Huth,[4] M. Incagli,[11] T. Ino,[16] H. Iso,[16] H. Jensen,[4] C. P. Jessop,[6] R. P. Johnson,[4] U. Joshi,[4] R. W. Kadel,[4] T. Kamon,[15] S. Kanda,[16] D. A. Kardelis,[7] I. Karliner,[7] E. Kearns,[6] S. Kim,[16] R. Kephart,[4] P. Kesten,[2] R. M. Keup,[7] H. Keutelian,[7] L. Kirsch,[2] K. Kondo,[16] S. E. Kuhlmann,[1] E. Kuns,[14] A. T. Laasanen,[12] J. I. Lamoureux,[18] W. Li,[1] T. M. Liss,[7] N. Lockyer,[10] C. B. Luchini,[7] P. Maas,[4] M. Mangano[11] J. P. Marriner,[4] R. Markeloff,[18] P. McIntyre,[15] A. Menzione,[11] T. Meyer,[15] L. A. Markosky,[18] R. Mattingly,[2] S. Mikamo,[8] M. Miller,[3] T. Mimashi,[16] S. Miscetti,[5] M. Mishina,[8] S. Miyashita,[16] Y. Morita,[16] S. Moulding,[2] A. Mukherjee,[4] Y. Muraki,[16] L. Nakae,[2] I. Nakano,[16] C. Nelson,[4] C. Newman-Holmes,[4] J. S. T. Ng,[6] M. Ninomiya,[16] L. Nodulman,[1] S. Ogawa,[16] R. Paoletti,[11] A. Para,[4] E. Pare,[6] J. Patrick,[4] T. J. Phillips,[6] R. Plunkett,[4] L. Pondrom,[18] J. Proudfoot,[1] G. Punzi,[11] D. Quarrie,[4] K. Ragan,[10] G. Redlinger,[3] J. Rhoades,[18] F. Rimondi,[19] L. Ristori,[11] T. Rohaly,[10] A. Roodman,[3] A. Sansoni,[5] R. D. Sard,[7] A. Savoy-Navarro,[19] V. Scarpine,[7] P. Schlabach,[7] E. E. Schmidt,[4] M. H. Schub,[12] R. Schwitters,[6] A. Scribano,[11] S. Segler,[4] Y. Seiya,[16] M. Sekiguchi,[16] P. Sestini,[11] M. Shapiro,[6] M. Sheaff,[18] M. Shochet,[3] J. Siegrist,[9] P. Sinervo,[10] J. Skarha,[18] K. Sliwa,[17] D. A. Smith,[11] F. D. Snider,[3] R. St. Denis,[6] A. Stefanini,[11] R. L. Swartz, Jr.,[7]

Submitted to Phys. Rev. D.

M. Takano,[16] K. Takikawa,[16] S. Tarem,[2] D. Theriot,[4] M. Timko,[15] P. Tipton,[9] S. Tkaczyk,[4] A. Tollestrup,[4] G. Tonelli,[11] J. Tonnison,[12] W. Trischuk,[6] Y. Tsay,[3] F. Ukegawa,[16] D. Underwood,[1] R. Vidal,[4] R. G. Wagner,[1] R. L. Wagner,[4] J. Walsh,[10] T. Watts,[14] R. Webb,[15] C. Wendt,[18] W. C. Wester, III,[9] T. Westhusing,[11] S. White,[13] A. Wicklund,[1] H. H. Williams,[10] B. Winer,[9] A. Yagil,[4] A. Yamashita,[16] K. Yasuoka,[16] G. P. Yeh,[4] J. Yoh,[4] M. Yokoyama,[16] J. C. Yun,[4] F. Zetti[11]

[1] *Argonne National Laboratory, Argonne, Illinois 60439*

[2] *Brandeis University, Waltham, Massachusetts 02254*

[3] *University of Chicago, Chicago, Illinois 60637*

[4] *Fermi National Accelerator Laboratory, Batavia, Illinois 60510*

[5] *Laboratori Nazionali di Frascati, Istituto Nazionale di Fisica Nucleare, Frascate, Italy*

[6] *Harvard University, Cambridge, Massachusetts 02138*

[7] *University of Illinois, Urbana, Illinois 61801*

[8] *National Laboratory for High Energy Physics (KEK), Tsukuba-gun, Ibaraki-ken 305, Japan*

[9] *Lawrence Berkeley Laboratory, Berkeley, California 94720*

[10] *University of Pennsylvania, Philadelphia, Pennsylvania 19104*

[11] *Istituto Nazionale di Fisica Nucleare, University and Scuola Normale Superiore of Pisa, I-56100 Pisa, Italy*

[12] *Purdue University, West Lafayette, Indiana 47907*

[13] *Rockefeller University, New York, New York 10021*

[14] *Rutgers University, Piscataway, New Jersey 08854*

[15] *Texas A&M University, College Station, Texas 77843*

[16] *University of Tsukuba, Ibaraki 305, Japan*

[17] *Tufts University, Medford, Massachusetts 02155*

[18] *University of Wisconsin, Madison, Wisconsin 53706*

[19] *Visitor*

A search for the top quark in $\bar{p}p$ collisions at a center of mass energy of 1.8 TeV using the Collider Detector at Fermilab is described. A study of events selected by requiring an energetic electron, missing transverse energy, and two or more jets excludes at 95% confidence level the Standard Model production and decay of $t\bar{t}$ pairs if the top quark mass is between 40 and 77 GeV/c^2. The observed electron + multijet data are consistent with W boson production.
14.80.Dq, 12.15.Ff, 13.85.Qk, 13.85.Rm

I. INTRODUCTION

The top quark (t quark) is postulated in the Standard Model as the SU(2) doublet partner of the bottom (or b) quark. Evidence for the existence of the top quark is found in various measurements of b quark production and decay: (i) the absence of flavor changing neutral currents in b quark decay rules out most models without a top quark[1]; (ii) a measurement of the forward-backward charge asymmetry for the process $e^+e^- \rightarrow b\bar{b}$ has verified the Standard Model weak isodoublet couplings for b quarks, implying the existence of an isospin partner, the top quark[2]; and (iii) the level of mixing measured in the B_d^0 system is inconsistent with the b quark being an SU(2) singlet.[3] We describe in this paper a search for the top quark in $\bar{p}p$ collisions at $\sqrt{s}$ = 1.8 TeV using the Collider Detector at Fermilab (CDF) at the Fermilab Tevatron Collider. A summary of the results of this study has been published previously.[4]

At the time we undertook this study, searches for t quarks at e^+e^- machines had yielded a lower limit of 28 GeV/c^2 on the top quark mass.[5] Searches for t quark production and decay in $\bar{p}p$ collisions at $\sqrt{s}$ = 630 GeV had placed a lower limit on the top quark mass of 41 GeV/c^2 at 95% confidence level.[6,7] Recent results place more stringent limits on the top quark mass. We have published the results of a search for the top quark by considering events with an electron and a muon in the final state, where we find $M_{top} > 72$ GeV/c^2 at 95% confidence level.[8] Results from experiments other than CDF have set top mass limits of 44.5 GeV/c^2 and 69 GeV/c^2 at 95% confidence level for e^+e^- and $\bar{p}p$ searches, respectively.[9,10] A comprehensive analysis of weak neutral current data and intermediate vector boson masses[11,12] provides an indirect upper limit on the top quark mass of $\sim$ 190 GeV/c^2 for a Higgs boson mass of 100 GeV/c^2.

Top quarks can be produced directly through QCD processes resulting in a $t\bar{t}$ pair or they may be produced through W boson production followed by the decay $W \rightarrow t\bar{b}$

(if kinematically allowed). A theoretical prediction[7] of the t quark cross section in $\bar{p}p$ collisions at $\sqrt{s} = 1.8$ TeV for both of these processes is shown in Fig. 1. Direct $t\bar{t}$ pair production is predicted to be the dominant source of top quarks for all top masses. We therefore concentrate on the detection of t quarks produced in $t\bar{t}$ pairs. Furthermore, we will consider the decay modes where one t quark decays semileptonically and the other hadronically. Assuming a semileptonic branching ratio of 1/9 for top quarks, this signature comprises about 15% of the $t\bar{t}$ rate for each lepton species considered. The fully hadronic decay modes have the highest rate (about 44% of the total), but the background from QCD multijet production is very high for the resulting event configurations. Requiring two leptons in the final state is a clean signal for $t\bar{t}$ events, but the rate is low (e.g., the branching fraction for $t\bar{t} \rightarrow e\mu X$ is $\sim 2.5\%$). The analysis we describe here requires the presence of a high-p_T electron, missing transverse energy, and hadronic jets as a signal for $t\bar{t}$ production.

We have assumed in this study the standard model semileptonic branching ratio of 1/9 for top quarks. If a charged Higgs scalar H^+ exists with mass such that the decay $t \rightarrow b + H^+$ is kinematically allowed, then the branching ratio of $t \rightarrow be\nu$ can be greatly suppressed,[13] thereby reducing the sensitivity of our search. We have, however, reported a limit on the top quark mass without making this assumption from an indirect measurement of the W boson width[14]; we exclude a top quark with $M_{top} < 35$ GeV/c^2 at 95% confidence level.

Sections II–V of this paper describe the CDF detector and the data samples used in our analysis. Our study uses a sample of inclusive electron events that we have selected by requiring the existence of at least one high quality electron candidate in each event. We discuss this selection in Sec. VI and estimate both the efficiency of the selection criteria and the non-electron background contained in the sample. We then study the kinematic properties of these events, such as electron transverse

energy, missing transverse energy, and electron isolation, and compare them with known physics processes. We then apply additional selection criteria to enhance the potential top quark signal (Sec. VII and Sec. VIII). We fit the transverse mass distribution of the data to that expected from W and top quark events to determine the number of top quark events observed (Sec. IX). Finally, we consider the systematic uncertainties on the observed rate of top quark events in Sec. X and derive a limit on the top quark mass in Sec. XI. We summarize our conclusions in Sec. XII.

II. THE DETECTOR

The Collider Detector at Fermilab (CDF) is a general purpose magnetic detector situated at the Tevatron Collider at Fermilab. An elevation view of the CDF detector is presented in Fig. 2. The detector has been described in detail elsewhere[15]; here we describe the components relevant to this analysis. [We will use a coordinate system in which z is measured from the center of the CDF detector along the proton beam, y is measured vertically, and x is measured horizontally. The variable r is the perpendicular distance to the beam ($r \equiv \sqrt{x^2 + y^2}$). The pseudorapidity variable is defined as $\eta \equiv -\ln(\tan\frac{\theta}{2})$, where θ is the angle measured from the proton beam.]

A. Tracking

A set of eight time projection chambers mounted around the beam pipe provide r-z tracking to a radius of 22 cm from the beam in the pseudorapidity region $|\eta| < 3.5$. This vertex time projection chamber (VTPC) presents less than 2% of a radiation length of material to tracks with $|\eta| < 1.5$. In this analysis a primary function of the VTPC was to locate the event vertex along the beam axis. The resolution on this measurement is $\sim$ 1–2 mm, depending on the track multiplicity. Another function of the VTPC was to provide information used in the identification of photon conversions

(see Sec. VI B).

A large cylindrical drift chamber provides charged particle tracking in the region $|\eta| < 1.2$. This central tracking chamber (CTC) has 84 sense wire layers arranged in nine superlayers extending to a radius of 1.3 m. Twenty-four layers of sense wires are tilted $\pm 3°$ with respect to the beam direction to provide stereo information. The CTC, operated in a 1.412 Tesla solenoidal magnetic field, yields a transverse momentum resolution of $\delta p_T/{p_T}^2 = 0.002\ (GeV/c)^{-1}$. The resolution is improved to $\delta p_T/{p_T}^2 = 0.0011\ (GeV/c)^{-1}$ by constraining track trajectories to pass through the beam position,[16] although this method was not employed for this analysis.

B. Calorimetry

The CDF calorimeter is divided into three sections of pseudorapidity, called the central, plug, and forward regions (see Fig. 2), providing coverage over the region $|\eta| < 4.2$. Each section consists of an electromagnetic calorimeter and a hadronic calorimeter. In this analysis the central region ($|\eta| < 1.1$) was used for primary electron identification, jets were identified in both the central and plug calorimeters, and missing transverse energy (which we precisely defined in Sec. VII C) was calculated using the full calorimeter out to $|\eta| < 3.6$.

A lead-scintillator sampling calorimeter 18 radiation lengths deep provides electromagnetic shower detection in the region $|\eta| < 1.1$. This central electromagnetic calorimeter (CEM) is segmented into 15° wedges in the azimuthal direction, with each wedge consisting of ten projective towers, each subtending $\sim .11$ units of pseudorapidity.

The CEM was calibrated in an electron test beam using electrons with momenta between 10 and 50 GeV/c, and Cesium sources are used to track the energy calibration to $\sim 2\%$. The energy resolution for electrons is given by

$$\sigma(E)/E = 13.5\%/\sqrt{E_T} \oplus 2.0\% \qquad (1)$$

where $E_T \equiv E \sin\theta$ is expressed in GeV, and the two terms are to be added in quadrature. We performed a more precise calibration of the CEM for the measurement of the Z mass[16] but we did not employ that calibration for this analysis.

A set of proportional wire chambers is located in the CEM at a depth of six radiation lengths to measure the position and shape of electromagnetic showers. These central strip chambers (CES) have wire and cathode strip readout providing independent reconstruction of showers in the z and azimuthal views. The resolution on the position of shower centroids from 25 GeV/c electrons is about 2.5 mm for both the azimuthal and z views.

Measurement of hadronic energy in the central region is provided by the central and endwall hadronic calorimeters (CHA/WHA). The CHA/WHA has approximately the same geometry and segmentation as the CEM and covers the same region of pseudo-rapidity ($|\eta| < 1.1$). The energy resolution is approximately $\sigma(E)/E = 80\%/\sqrt{E_T}$. The CHA/WHA photomultiplier tubes are instrumented with TDC's that provide timing information used to reject out-of-time backgrounds, such as cosmic rays or particles from the Main Ring, the original Fermilab accelerator that now serves as an injector for the Tevatron and which passes over the detector.

The plug and forward calorimeters extend the calorimetric coverage to $|\eta| < 4.2$. These consist of layers of lead or iron planes instrumented with gas proportional chambers. Cathode pad readout of these calorimeters form projective towers of size $\Delta\eta \times \Delta\phi \sim 0.09 \times 0.087$. The energy resolution for the gas calorimeters is approximately $\sigma(E)/E = 30\%/\sqrt{E_T}$ and $\sigma(E)/E = 120\%/\sqrt{E_T}$ for electrons and jets, respectively.

III. THE TRIGGER

The CDF trigger is a four level system, the first three (Level-0 through Level-2) consisting of dedicated hardware processors, and the fourth (Level-3) consisting of a set of general-purpose microprocessors executing algorithms encoded in FORTRAN.

The Level-0 trigger consists of a set of scintillation counters at $3.2 < |\eta| < 5.9$ that is used to detect inelastic $\bar{p}p$ interactions. The Level-1 trigger decision is typically based on energy sums from the calorimeter. Energy clustering and track finding are performed by the Level-2 trigger. Finally, sophisticated software algorithms are run in the Level-3 processors, employing more advanced energy clustering, track finding, and shower clustering in the central strip chambers.

We required the events used in this analysis to pass an inclusive electron trigger. This trigger requires an electromagnetic (EM) cluster in the central region with $E_T >$ 12 GeV, with the ratio of hadronic to EM energy, $had/em < 0.125$. A CTC track pointing to the cluster (in the r-ϕ view) with $p_T > 6$ GeV/c is also required. The lateral energy profile of the electron candidate cluster is required to be consistent with an electron shower. Details of the electron clustering and lateral profile measurement can be found below in Sec. VI A. We have measured the efficiency of this trigger by studying electron candidate events that have been selected by an independent trigger. The behavior of the electron trigger near threshold ($10 < E_T < 20$ GeV) has been characterized by studying events passing an electron trigger with a lower (7 GeV) E_T threshold. We have found the 12 GeV electron trigger to be $98 \pm 0.5\%$ efficient for electrons passing the offline selection criteria described in Sec. VI A.

IV. DATA COLLECTION

The data set for this analysis was obtained during a one-year run of the Tevatron in 1988 and 1989. We collected an event sample corresponding to an integrated

luminosity of 4.4 pb^{-1}, of which about 6 million events were recorded to tape. The uncertainty of the integrated luminosity is at present estimated to be $\pm 15\%$. A fast offline pre-filter reduced this sample by a factor of about twenty by imposing loose electron cuts. The major reduction was obtained by the requirement of a track with p_T of at least 10 GeV/c pointing at the electron cluster. The selection criteria described below (Sections VI and VII) further reduced this sample by another factor of about 2500.

V. MONTE CARLO DATA SETS

We discuss in this section the Monte Carlo data sets to which we will refer in subsequent sections. We generated Monte Carlo event samples for $t\bar{t}$, b and c quark, and W + jet production processes. We passed all Monte Carlo events through a full simulation of the CDF detector, including effects such as cracks, photon conversions and detector resolution. After simulation, the events were passed through the offline reconstruction in the same way as the real data. The event selection criteria applied to the real data were then applied to the reconstructed events, except for an algorithm which rejects electrons coming from photon conversions (see Sec. VI B). The effect of this algorithm on prompt electrons has been calculated and the Monte Carlo efficiencies have been corrected accordingly.

The ISAJET[17] Monte Carlo program was used to generate $t\bar{t}$ events for top masses (M_{top}) of 40, 50, 60, 70, 75 and 80 GeV/c^2. The integrated luminosities of the $t\bar{t}$ samples were 3.6, 3.6, 7.0, 13.0, 44.1, and 21.9 pb^{-1} for these event samples, respectively. We used the $t\bar{t}$ production cross section calculated by Altarelli *et al.*,[7] which is based on the QCD total cross section formulas for heavy quark production, complete through order α_s^3, by Nason *et al.*[18]

ISAJET was also used to generate a sample of b and c quark events. All species of

partons were included in this calculation, although requiring an electron with $p_T > 10$ GeV/c^2 in the event effectively selects only semileptonic decays of b and c quarks. Production of b quarks via the mechanisms of (i) direct $b\bar{b}$ production (e.g. $gg \rightarrow b\bar{b}$), (ii) gluon splitting (e.g. $gg \rightarrow gg, g \rightarrow b\bar{b}$), and (iii) flavor excitation ($gb \rightarrow gb$) are included in this calculation. Because this calculation is very CPU intensive, the sample generated for this analysis is limited to an integrated luminosity of 600 nb^{-1}.

We have found that ISAJET does not accurately reproduce the jet activity in $W^{\pm}$ and Z^0 events. For this reason, we used the PAPAGENO[19] program to generate events for the process $p\bar{p} \rightarrow W + \text{jets} + X$. The PAPAGENO Monte Carlo generator performs a W + n jets calculation[20] that includes all relevant tree-level diagrams. The partons generated by PAPAGENO are fragmented into hadrons following the method employed by ISAJET, using fragmentation parameters that have been adjusted to agree with CDF tracking data. An underlying event is generated using a modified version of the model used by ISAJET. The E_T scale of the underlying event (i.e. the amount of energy detected in the event that is not associated with the hard scattering process) was tuned to CDF data. The following parameters were used to generate the W + 2 jet sample: (i) electron $p_T > 12$ GeV/c, (ii) parton $p_T > 8$ GeV/c, and (iii) $\Delta R \equiv \sqrt{(\Delta\eta)^2 + (\Delta\phi)^2} > .65$ between any two partons. The W + 2 jet sample corresponds to an integrated luminosity of 41.3 pb^{-1}, according to PAPAGENO's prediction for the cross section. We also generated a sample of W + 1 jet events, corresponding to an integrated luminosity of about 5 pb^{-1}.

VI. INCLUSIVE ELECTRON SELECTION

We began the top quark search by selecting a sample of inclusive electrons. We estimate both the efficiency of the selection criteria and the non-electron background contained in the sample. We then study the kinematic properties of these events,

such as electron transverse energy, missing transverse energy, and electron isolation, and compare them with known physics processes.

A. Selection Criteria

We select electron candidates by requiring a cluster of electromagnetic energy associated with a CTC track in the central region. The energy cluster is required to have the correct shower profiles (both in the calorimeter and in the strip chambers) and the track must match the cluster both in position and momentum.

The algorithm used to define electromagnetic energy clusters considers all "seed" towers with at least 3 GeV of electromagnetic transverse energy. Adjacent towers are added to the cluster if their $E_T > 0.1$ GeV. In the central calorimeter an electron shower is generally contained within one or two towers. Furthermore, the border between towers in the ϕ direction contains roughly 1 cm of inactive material, which effectively prevents energy from a single shower crossing the ϕ boundary between towers in the central region. For these reasons, the size of central EM clusters is restricted to three or fewer adjacent towers with a common ϕ. In the subsequent analysis, we only consider electromagnetic clusters that have $had/em < 0.1$.

We require the electromagnetic cluster to have transverse electromagnetic energy $E_T^{em} > 15$ GeV. Real electrons are expected to have little leakage into the hadronic compartment of the calorimeter, so we impose the cut $had/em < 0.05$. We define a variable, $\mathcal{L}_{shr}$, which is a measure of the lateral shower profile for electron candidates in the central region:

$$\mathcal{L}_{shr} = 0.14 \sum_k \frac{M_k - P_k}{\sqrt{0.14^2 E + (\Delta P_k)^2}} \tag{2}$$

where the sum is over towers in the cluster adjacent to the seed tower, M_k is the measured energy in the adjacent tower, P_k is the expected energy in the adjacent tower, E is the electromagnetic energy in the cluster, and ΔP_k is an estimate of

the error in P_k. The expected energy P_k is predicted using the the event vertex, the center of the shower as measured in the central strip chamber and a shower profile parametrization obtained from test beam measurements. The uncertainty in this quantity, ΔP_k, is taken to be the variation in P_k arising from a 1 cm ($\sim 2\sigma$) shift in the center of the shower, while the first term in the denominator comes from the resolution of the central electromagnetic calorimeter. We impose the condition $\mathcal{L}_{shr} < 0.2$; the efficiency of this and the other electron selection criteria are discussed in Sec. VI C below.

The strip chambers imbedded in the CEM locate the showers more precisely in both the z and r-ϕ directions, and provide a detailed measurement of the shower profile. We reconstruct electromagnetic showers independently in the two views of the strip chambers and fit the resulting profiles to a parametrization of the profiles obtained from test beam electrons. We require the values of χ^2 obtained from the fits to satisfy $\chi^2_z < 10$ and $\chi^2_\phi < 10$.

We require a track pointing at the electron candidate and impose cuts on position and energy matching to significantly reduce non-electron backgrounds. CTC tracks are extrapolated to the radius of the strip chambers and the extrapolated position is compared with the shower location defined by the strip clusters. The cuts $|\Delta z| < 3$ cm and $|\Delta x| < 1.5$ cm are made, where

$$\Delta z = z_{CES} - z_{CTC} \tag{3}$$

$$\Delta x = x_{CES} - x_{CTC} \tag{4}$$

and x is the distance from the wedge center in the azimuthal direction. The cut is tighter in the x direction due to the better CTC resolution in that view. We impose an energy-momentum match between the calorimeter cluster and CTC track

by requiring the ratio of the energy in the cluster to the track momentum (E/p) to be less than 1.5.

Table I summarizes the electron cuts. Figures 3 and 4 show distributions for the electron variables. For each distribution cuts are made on all variables except the one being plotted, except for the χ^2_Z and $\mathcal{L}_{shr}$ histograms, which already show the cut applied.

We impose calorimeter fiducial cuts on the electron candidates to ensure that the electromagnetic shower is well measured. Electron candidates are required to be at least 2.5 cm from the ϕ-boundaries between wedges of the central calorimeter (1 cm inside the active region of the strip chambers) and at least 9 cm away from a crack at $\theta = 90°$ (3 cm inside the active region of the strip chambers). Candidates that impact the outermost set of towers (at $\eta \sim \pm 1.1$) in the CEM calorimeter are also rejected, because for mechanical reasons these towers have fewer radiation lengths than the other CEM towers. Finally, an event is rejected if the z-coordinate of the primary vertex is more than 60 cm away from the center of the detector. This cut is made to insure that all jets are well contained in the calorimeters.

We find 16 598 electron candidates that survive this selection.

B. Removal of Conversion Electrons

A significant source of electrons are Dalitz decays of π^0's ($\pi^0 \rightarrow \gamma e^+ e^-$) and photons that interact in the material of the detector to produce an e^+e^- pair; we refer to both processes as "conversions." An electron arising from a conversion will usually be accompanied by a second track reconstructed in the CTC that forms a very low electron pair mass with the electron candidate track.

We form the pair mass for the electron candidate and all oppositely charged tracks within 30° of the candidate track, retaining the pair that results in the lowest mass.

We calculate the pair mass at the point of closest approach to both track trajectories projected onto the $r-\phi$ plane. The distribution of the mass calculated in this way will generate a peak displaced from zero for the conversions in our sample. Figure 5(a) shows the invariant mass distribution of such track pairs for all electron candidates. The large peak near zero is indicative of conversions.

Some conversions may also be identified using the tracking information in the vertex chamber (VTPC). If a conversion occurs at a radius greater than that of the outer radius of the VTPC, there will be an absence of hits along the track path in the vertex chamber. Figure 5(b) shows the variable f_{VTPC}, defined as the number of VTPC hits found along the track path, divided by the number of hits expected. The excess at zero is due to conversions that occur outside the volume of the VTPC, which we will call "outer conversions". Conversions that occur inside the VTPC's inner radius, and therefore leave hits in the VTPC, will be called "inner conversions". Electrons arising from conversions are removed by rejecting electron candidates for which

$$m_{ee} < 0.5 \text{ GeV/c}^2 \text{ or } f_{VTPC} < 0.2. \tag{5}$$

Outer conversions are removed by both the f_{VTPC} cut and the m_{ee} cut. Inner conversions leave a track in the VTPC and therefore can only be removed by the mass cut.

We have estimated the efficiency of these cuts for removing real conversions, and the over-efficiency for removing prompt electrons from our data. We first note that virtually all tracks passing through the VTPC will leave at least 20% of the expected hits, i.e., no prompt electron will be rejected by the f_{VTPC} cut. This has been verified by studying a sample of electrons from Z^0 decays (we estimate that of order 1% of prompt electrons fail the f_{VTPC} cut). The second observation is that virtually all electron candidates that fail the f_{VTPC} cut are outer conversions. Thus the outer

conversions form a sample of electrons that result entirely from photon conversions in the material surrounding the VTPC. We then determine: (i) the fraction of good electrons removed by the cuts, f_{prompt}; (ii) the efficiency for removing real conversions, ϵ_{conv}; and (iii) the fraction of the final sample attributed to unidentified conversions, f_{bg}.

The fraction of prompt electrons removed by the cuts, f_{prompt}, is equal to the probability that a high-p_T electron candidate track together with a second uncorrelated track forms a pair mass less than 0.5 GeV/c^2. We estimate this probability by considering how often like-sign pairs of tracks result in a low pair mass. Since the populations of like-sign and unlike-sign tracks near electron candidates in our sample are equal, we can write

$$f_{prompt} = \frac{n_{i,ls}}{n_{i,ele}}, \tag{6}$$

where $n_{i,ls}$ is the number of electron candidates that have $f_{VTPC} > 0.2$ and $m_{ee} <$ 0.5 GeV/c^2, using pairs of like-sign tracks. The denominator, $n_{i,ele}$, is the total number of electron candidates with $f_{VTPC} > 0.2$. We find $f_{prompt} = 0.101 \pm 0.004$ for our inclusive electron sample. The uncertainty in f_{prompt} reflects the finite size of the sample and the uncertainty in the ratio of like-sign to unlike-sign tracks near the electron candidate.

We estimate the efficiency of the mass cut for identifying conversions using the 1604 electrons that have $f_{VTPC} < 0.2$ (*i.e.* the outer conversions). Of this sample, 1310 candidates also have $m_{ee} < 0.5$ GeV/c^2, yielding an efficiency for the m_{ee} cut of

$$\epsilon_{mass} = \frac{1310}{1604} = 0.817 \pm 0.050. \tag{7}$$

The uncertainty in ϵ_{mass} reflects the systematic error we have made by ignoring the small contribution of prompt electrons to the outer conversion sample. Of the 14 994 electron candidates with $f_{VTPC} > 0.2$, 3719 of them have $m_{ee} < 0.5$ GeV/c^2 and are

also tagged as conversions, leaving a prompt electron sample of 11 275 events. The total number of real electrons, n_e, and the number of conversions not removed with the f_{VTPC} cut, n_i, then satisfy the following set of equations:

$$3719 = f_{prompt}\, n_e + \epsilon_{mass}\, n_i \tag{8}$$

$$11\ 275 = (1 - f_{prompt})\, n_e + (1 - \epsilon_{mass})\, n_i. \tag{9}$$

We solve these equations and find $n_e = 11\ 914$ and $n_i = 3080$.

With this information, we can estimate the number of unidentified conversion electrons remaining in this sample by

$$n_{bg} = (1 - \epsilon_{mass}) \times n_i, \tag{10}$$

which yields 564 unidentified conversions. Hence, the fraction of the final sample attributed to unindentified conversions is $f_{bg} = 0.050 \pm 0.015$. The overall conversion detection efficiency is

$$\epsilon_{conv} = \frac{n_o + \epsilon_{mass} n_i}{n_o + n_i} = 0.88 \pm 0.04, \tag{11}$$

where n_o is the number of outer conversions identified by the f_{VTPC} cut. A summary of the results of the conversion analysis is presented in Table II.

C. Electron Selection Efficiency

We determine the electron selection efficiency using Monte Carlo data and a sample of electrons from Z^0 decays in the data. We select the sample of Z^0 events by requiring an electron candidate passing the selection criteria plus another electromagnetic cluster in the central region such that the pair form a mass between 80 and 105 GeV/c^2. We also require the first electron to satisfy $E_T^{em} > 20\ GeV$. The second cluster must have $E_T^{em} > 20\ GeV$ and a track pointing to it with $p_T > 10$ GeV/c. Finally, a very loose isolation cut is placed on both electrons to reduce any remaining background,

$$E_T^{cone} - E_T^{em} < 12\ GeV, \tag{12}$$

where E_T^{cone} is the energy in a cone of radius 0.4 in η–ϕ space, centered on the electron cluster. The electron efficiency is determined by measuring the number of second electrons that pass the selection. If N_Z is the number of Z^0's in the sample and N_2 is the number of second electrons that pass the cuts, then the efficiency of the cuts is given by

$$\epsilon = \frac{2\,N_2}{N_Z + N_2}. \tag{13}$$

The efficiency for a single cut (ϵ_c) is given by

$$\epsilon_c = \frac{\epsilon}{2}\left(1 - \frac{N_c}{N_Z}\right) + \frac{N_c}{N_Z}, \tag{14}$$

where ϵ is given in Eq. (13) above and N_c is the number of second electrons which pass the cut in question. The results of this analysis are presented in Table III. We also show in Table III the results obtained from a Monte Carlo sample of $Z^0 \to e^+e^-$ events. There is good agreement between the data and Monte Carlo sample in all cases except perhaps for the efficiency of the E/p cut, where the discrepancy is about 1.5 times the statistical uncertainty. In particular, the agreement in the overall efficiency is good. A similar study using electrons from $W^{\pm}$ decays yields consistent results.

D. Backgrounds in the Inclusive Electron Sample

Non-electron background in the electron sample comes primarily from photon conversions and from charged pions that deposit nearly all of their energy in the electromagnetic compartment of the calorimeter. Since the p_T of tracks in the central region are well measured, backgrounds from low p_T charged pions overlapping a high p_T neutral electromagnetic shower from a π^0 or a photon are negligible.

We remove electrons arising from photon conversions and the Dalitz decay $\pi^0 \to$

γe^+e^- from the sample as discussed above (see Sec. VI B). The remaining conversion background is estimated to be $5.0 \pm 1.5\%$ of the inclusive sample (see Table II).

Charged pions whose showers are contained in the electromagnetic compartment of the calorimeter form the other significant background to prompt electrons. We estimate the size of this background by comparing the relative number of electron candidates that have $had/em < 0.05$ after all the other electron cuts have been made to the total number of candidates with $had/em < 0.1$; pions that pass the other electron cuts have an approximately flat had/em distribution over $had/em < 0.1$ whereas electrons have a had/em distribution sharply peaked below $had/em < 0.05$. This method may overestimate the interacting $\pi^{\pm}$ background because it does not differentiate between showers initiated by a $\pi^{\pm}$ and those initiated by a prompt electron where a low energy hadron has deposited energy in the hadronic compartment behind the electromagnetic shower. Studies of the energy flow around the electron candidates indicate that the number of such prompt electrons is relatively small, but we have not attempted to distinguish between these two classes of electron candidates.

Let N_p and N_f be the number of events that have $had/em < 0.05$ and $0.05 < had/em < 0.1$, respectively, and let ϵ_e and ϵ_π be the fraction of candidates that have $had/em < 0.05$ for electrons and charged pions, respectively. We can determine the total number of real electrons, N_e, and real charged pions, N_π in the sample before the had/em cut is applied by solving the two equations:

$$N_p = \epsilon_e N_e + \epsilon_\pi N_\pi, \tag{15}$$

$$N_p + N_f = N_e + N_\pi. \tag{16}$$

We have determined the fraction $\epsilon_\pi = 0.57 \pm 0.10$ from test beam studies. The efficiency for electrons was determined by considering electrons selected by the conversion

algorithm. We only consider conversion candidates which have $1 < E/p < 1.1$, to reduce the probability that the conversion electron is accompanied by an extra electron or photon that could distort the *had/em* distribution. The efficiency of the *had/em* cut for electrons is thus determined to be $\epsilon_e = .95 \pm .02$. This efficiency is somewhat lower than that determined using Z^0 events (Sec. VI C), which we ascribe to the fact that typical conversion electrons are less isolated than electrons from Z^0 (or $W^{\pm}$) decay (in a conversion event it is more likely that additional hadronic energy will accompany the electron's energy, thereby increasing the *had/em* ratio).

The size of the charged pion background expressed as a fraction of the inclusive electron sample is then

$$f_{bg}^{\pm} = \frac{\epsilon_\pi N_\pi}{N_p} = 20 \pm 10\%. \tag{17}$$

The details of the calculation are provided in Table IV.

In summary, we find the inclusive electron sample to contain backgrounds from photon conversions and charged pions of $5.0 \pm 1.5\%$ and $20 \pm 10\%$, respectively, resulting in a combined background that is estimated to be

$$f_{bg}^{tot} = 25 \pm 10\%. \tag{18}$$

E. Summary of inclusive selection

The selection criteria described above yield an inclusive electron sample of 11 275 electron candidates in 11 157 events. These electron candidates have $E_T^{em} > 15$ GeV and $|\eta| < 1.1$. We have estimated the non-electron background in this sample to be $f_{bt}^{tot} = 25 \pm 10\%$, where approximately 80% of the background is from charged pions and the remaining background is due to unidentified conversion electrons. Additional selection criteria to help enhance a possible top quark signal are discussed in the next section.

VII. ELECTRON + JETS SELECTION

In the decay

$$t \to be\nu$$

the electron and the neutrino are typically produced with high transverse energy. The neutrino transverse energy usually manifests itself as a significant amount of missing transverse energy in the event. The missing E_T (or $\not\!\!E_T$) is defined by

$$\not\!\!E_T = \left|\vec{\not\!\!E}_T\right| = \left|-\sum_i E_{T_i}\hat{n}_i\right| \tag{19}$$

where E_{T_i} is the transverse energy in the i^{th} calorimeter tower and $\hat{n}_i$ is a unit vector directed from the event vertex to the tower in the $r-\phi$ plane. The sum is over all calorimeter towers with $|\eta| < 3.6$. We do not correct the missing E_T for calorimeter non-linearities. The scatterplot of $\not\!\!E_T$ vs E_T^{em} for the inclusive electron sample is shown in Fig. 6 (only about 2 pb^{-1} of data are shown for clarity). There is a large cluster of events with high E_T^{em} and high $\not\!\!E_T$, as expected for W events where $W \to e\nu$. Also, Z production is evident in the events with high E_T^{em} and low $\not\!\!E_T$. The majority of the inclusive electron events are clustered at low values of E_T^{em} and $\not\!\!E_T$, where one expects to find semileptonic decays of b and c quarks and fake electron events. All of these processes form backgrounds to a potential top signal.

We discuss in this section the additional cuts used to define a potential top quark sample. We reduce the background from b and c quark production by imposing an isolation requirement on electrons. Z^0 candidates are explicitly removed by rejecting events with high-mass electron pairs, and the background from $W^{\pm}$ production is reduced by requiring several jets in the events. Finally, stricter cuts on E_T^{em} and $\not\!\!E_T$ are imposed to further reduce the backgrounds from b and c quark production and fake electrons to negligible levels.

A. Isolation

A majority of the electron candidates in the inclusive electron sample have E_T^{em} and $\not\!\!E_T$ less than 20 GeV (see Fig. 6). We have compared the inclusive electron data with the sample of Monte Carlo b and c quark events (see Sec. V for a discussion of the Monte Carlo sample). For this comparison $W^{\pm}$ bosons have been removed from the inclusive electron data by requiring the transverse mass ($M_T^{e\nu} \equiv \sqrt{2\,E_T^{em}\,\not\!\!E_T\,(1-\cos\Delta\phi_{e\nu})}$, where $\Delta\phi_{e\nu}$ is the azimuthal difference between the electron and $\not\!\!E_T$ vectors) to be less than 40 GeV/c^2. The rate of observed events with $E_T^{em} < 20\ GeV$ is consistent with the ISAJET Monte Carlo prediction for these processes although the theoretical prediction has large uncertainties. Distributions such as the electron and leading and non-leading jet E_T spectra show good agreement with the Monte Carlo prediction (see Fig. 7). We have studied the jet spectra as a function of electron E_T, and have found agreement in the average jet E_T between data and Monte Carlo to better than 1.5 GeV over the range $12 < E_T^{em} < 20$ GeV (we dicsuss our definition of jets in Sec. VII C).

Furthermore, the energy flow around the electron is well modeled by the Monte Carlo. The isolation of an electron can be quantified by E_T^{iso}, defined as the sum of the transverse energy in calorimeter towers immediately adjacent to the electron cluster. Figure 8 shows the distribution of E_T^{iso} for electrons with $E_T^{em} < 20$ GeV along with the ISAJET prediction for b and c quark production. The distribution from the data agrees well with the b and c quark calculation in the region $E_T^{iso} > 0.5$ GeV. Some residual $W^{\pm}$ and Drell-Yan events can be seen at very low E_T^{iso}. Also shown is the expected distribution for electrons from t quark decay, which are seen to be significantly more isolated. Because of the residual $W^{\pm}$ and Drell-Yan events in the data at low E_T^{iso}, the Monte Carlo curve for b and c quark production has been normalized to the data in the region above 0.5 GeV. The $t\bar{t}$ curve has arbitrary

normalization. We impose the cut

$$E_T^{iso} < 2\ GeV \tag{20}$$

to reduce these backgrounds to a possible top signal. The efficiency of this criterion for top quark events varies from 86–90% for M_{top} in the range 40–80 GeV/c^2. We estimate that it removes about 55% of the b and c quark events. There are $\sim$ 7500 events that survive the isolation requirement.

B. Z Boson Removal

Events containing a Z^0 boson decaying to an e^+e^- pair give rise to high-p_T electrons, which may contribute to the background in the top sample. We removed such events by selecting on the invariant mass formed by the electron candidate with all other electromagnetic clusters in the event. Figure 9 shows this distribution for the inclusive isolated electron sample. We rejected events that contained a pair with mass greater than 70 GeV/c^2. This cut effectively removes all Z^0 events in the sample, and the Monte Carlo efficiency for top events is greater than 99% for $M_{top} = 40$ GeV/c^2 and 96% for $M_{top} = 80$ GeV/c^2.

C. Jets

Four quark jets are typically expected in a $t\bar{t}$ event when one of the t quarks decays semileptonically and the other hadronically. Conversely, most W's are produced with little associated jet activity. Requiring the presence of several jets in the event significantly reduces the background from $W^{\pm}$ and Z^0 boson decays and (to a lesser extent) from b and c quark decay. We discuss here the jet cluster algorithm used to form jet clusters, jet energy scales and detection efficiency, and finally the jet cuts applied to the isolated electron sample.

1. Jet Clustering

We detect jets as clusters of energy in the calorimeter, using a fixed-cone clustering algorithm. Preclusters are defined as contiguous sets of adjacent towers with $E_T > 1$ GeV. Clusters are formed from preclusters by considering all the towers within a cone in η-ϕ space of radius 0.7 centered on the precluster. All towers with $E_T > 0.1$ GeV within the cone are included in the cluster. The centroid of the cluster, defined as the E_T-weighted average, is calculated and the cone is repositioned on the centroid. Again, towers within the new cone passing the E_T cut are included in the cluster. This procedure is repeated until the towers in the cluster do not change.

If a cluster is completely contained in a larger cluster, the smaller one is dropped. Partially overlapping clusters may be merged together, depending on the overlap fraction, defined as the E_T in the overlap region divided by the E_T in the smaller cluster. If the fraction is above 0.75, the two clusters are combined. Otherwise, the towers in the overlap region are divided between the two clusters according to their proximity to the cluster centroid. After this division, the centroids are re-calculated and the towers in the original overlap region are re-divided based on their distance from the new centroids. This procedure is iterated until a stable configuration is reached.

2. Jet Energy Scale and Detection Efficiency

We used the following procedure to model the response of the detector to jets. The central calorimeter simulation was tuned on CDF test beam data, using pions with momenta between 15 and 150 GeV/c, and electrons with momenta between 10 and 50 GeV/c. We adjusted the simulation to give the correct response in both the "face" and "crack" regions of the calorimeter, where the crack region is defined to be the

calorimeter tower face within 2° in azimuth of a tower boundary. The response to lower energy pions (0.5 to 10 GeV) was determined *in situ* by considering isolated charged tracks in minimum bias events. In this case, we determined the calorimeter response using the transverse momentum as reconstructed in the central tracking chamber (a correction was made for the neutral energy accompanying the track). We estimate the systematic uncertainty in the jet energy scale for central jets with observed transverse energy between about 18 and 180 GeV to range from 13% for the lower energy jets to 5% for the higher energy jets.

We verified the jet energy scale by considering direct photon production, which is dominated by a high-p_T photon recoiling against a single parton. We selected direct photon events by requiring an electromagnetic shower in the central calorimeter without a track pointing to it. We rejected photons from π^0 decay by requiring that the shower profile in the central strip chambers be an excellent fit to a parametrization of test beam showers (we required $\chi^2 < 4$ for the fit with typically a few degrees of freedom). We required the photon to be isolated, with no other clusters with $E_T > 3$ GeV in the same hemisphere.

In these events, the transverse momentum of the photon balances the p_T of the recoil parton. Thus, a comparison between the photon E_T and the E_T of the leading jet in the opposite hemisphere allows one to determine the efficiency for detecting jets above some E_T threshold as a function of parton p_T. A comparison between the direct photon data and an ISAJET calculation shows the jet energy scale in the simulation to agree with the data within a few percent. Figure 10 shows the probability for finding a jet cluster with observed $E_T > 10$ GeV in the hemisphere opposite the photon as a function of the parton transverse momentum. The Monte Carlo prediction is shown as the solid curve. The agreement in the jet detection efficiency implies that the detector simulation correctly models the energy response of the calorimetry to jets

within a few percent.

Further confidence in the jet energy scale comes from the comparison of jet E_T spectra in the inclusive electron sample with the Monte Carlo calculation for b and c production, as discussed above (see Sec. VII A). Based on these studies we conservatively estimate the systematic uncertainty in the Monte Carlo jet energy scale to be 20% for a jet with an E_T of 10 GeV.

3. Jet Selection Criteria

We required events for the electron + jets sample to have two or more jets with each jet having at least 10 GeV of observed energy. Furthermore, because the pseudorapidity distribution of jets from $t\bar{t}$ production is significantly narrower than that from $W^{\pm}$ or b quark production (see Fig. 11), we required the jets to have $|\eta_{jet}| < 2$. This cut was made on the pseudorapidity of the jet as determined from the center of the detector to ensure that the jets were contained in the central or plug calorimeter, rather than the event origin.

VIII. KINEMATIC CUTS - FINAL SAMPLE

Electrons and neutrinos from top quark decay typically have transverse energies greater than 15 GeV. We therefore make tighter cuts on E_T^{em} and $\not\!\!E_T$ to define our final event sample. We then discuss the backgrounds to top in the final sample.

A. "Loose" and "Tight" Kinematic Cuts

We show the scatterplot of $\not\!\!E_T$ vs E_T^{em} for the 922 events in the electron + 2 jet sample in Fig. 12(a) (we use "electron + 2 jets" to signify an event with an electron plus two or more jets). This can be contrasted with the expected $\not\!\!E_T$ vs E_T^{em} plot for $t\bar{t}$ production for a top mass of 70 GeV and for W + 2 jet production shown in

Figs. 12(b) and (c), respectively. These scatterplots (and all scatterplots of Monte Carlo data in the report) have not been normalized to the data; their equivalent integrated luminosities are given in Sec. V. In the region of high E_T^{em} and $\not\!\!E_T$ the data resemble W events. Also, there are a large number of events in the data, clustered at low E_T^{em} and $\not\!\!E_T$, that cannot be interpreted as resulting from W production. We present in Fig. 13(a) the distribution of $\not\!\!E_T$ vs E_T^{em} for events identified as conversion candidates, a sample which has characteristics similar to the QCD background present in the data. Figure 13(b) shows the same distribution for non-isolated electron + 2 jet events ($E_T^{iso} > 2$ GeV), a sample enriched in events from b quark production. Both samples of events cluster at low values of $\not\!\!E_T$ and E_T^{em}. To further reduce the backgrounds from b and c quark production and QCD processes, the following kinematic cuts are made on E_T^{em} and $\not\!\!E_T$, (hereafter referred to as "loose" cuts):

$$\begin{aligned} E_T^{em} &> 15 \text{ GeV} \\ \not\!\!E_T &> 15 \text{ GeV} \\ E_T^{em} + \not\!\!E_T &> 40 \text{ GeV}. \end{aligned} \tag{21}$$

There are 123 electron + 2 jet events that survive the loose kinematic cuts. When making comparisons to the predictions for higher top masses stricter kinematic cuts are applied (referred to as "tight" cuts):

$$\begin{aligned} E_T^{em} &> 20 \text{ GeV} \\ \not\!\!E_T &> 20 \text{ GeV}. \end{aligned} \tag{22}$$

There are 104 events that pass the tight cuts. The efficiencies of these kinematic cuts for t quark events have been determined from Monte Carlo data and are shown in Table V for various top masses. The contours of these two sets of kinematic cuts are shown in Fig. 12.

B. Backgrounds in the Final Sample

We estimate the background due to b and c quark production and QCD fake electrons in our final sample by considering the effect of the isolation (E_T^{iso}) cut. The method is similar to that applied to the case of the charged pion background in the inclusive electron sample where the *had/em* distribution was used to estimate the size of that background (see Sec. VI D). We assume that all the electrons in the sample result either from W decays or from the sources of non-isolated electrons previously mentioned; since the isolation of electrons from t quark decays is similar to that from $W^{\pm}$ decays, this approximation is valid even if there is a significant amount of top in the sample. Equations (15) and (16) can be used with the substitutions $e \leftrightarrow W$ and $\pi \leftrightarrow b$. Now ϵ_W and ϵ_b are the efficiencies of the E_T^{iso} cut for electrons from $W^{\pm}$ decay and non-isolated sources, respectively. The efficiency of the E_T^{iso} cut for W + jet events is found to be $\epsilon_W = .93 \pm .02$ from studies of Monte Carlo data and of a sample of W events that have very high missing E_T and that pass a loose electron selection. The efficiency for non-isolated electron candidates is found to be $\epsilon_b = .33 \pm .05$ from studies of E_T^{iso} for events with low $\not\!\!E_T$, conversion electron candidates, and candidates passing all the electron selection criteria except the *had/em* cut. N_W and N_b are the calculated numbers of real $W^{\pm}$'s and non-isolated electrons in the sample, before applying the E_T^{iso} cut. The results are shown in Table VI.

We estimate the background due to conversions and charged pions in the final sample using the same techniques described in Sec. VI D. The conversion detection efficiency varies with electron E_T and is shown in Table VII. Also shown is the amount of background remaining in a sample with a given E_T^{em} threshold. The loose and tight kinematic cuts correspond to E_T^{em} of 15 GeV and 20 GeV, respectively. For the charged pion background in the final sample, we consider the number of events that pass all the final cuts except the *had/em* cut. For the loose cuts we

find the number failing, $N_f = 6$, which gives a background fraction of $0.0 \pm 3.2\%$. Four events fail the *had/em* using the tight cuts, giving a background fraction of $0.0 \pm 4.8\%$. These non-electron background estimates for the final sample are summarized in Table VIII. We attribute the difference between the non-isolated electron background estimate and the background estimates from conversions and interacting $\pi^{\pm}$'s to residual backgrounds from b and c quark production.

1. W + jets

Based on the distribution of E_T and $\not\!\!E_T$, the electron + 2 jet data appear to be consistent with arising primarily from the W + 2 jet process. In this section we present comparisons of the data and the W + 2 jet Monte Carlo sample for several other characteristic variables. We interpret the missing E_T as the p_T of an undetected neutrino. The transverse momentum of the (real or virtual) W boson ($p_T^{e\nu}$) is then given by the magnitude of the vector sum of E_T^{em} and $\not\!\!E_T$:

$$p_T^{e\nu} = \left| \vec{E}_T^{em} + \vec{\not\!\!E}_T \right| . \tag{23}$$

The scatterplot of $M_T^{e\nu}$ vs $p_T^{e\nu}$ for the electron + 2 jet sample with loose cuts is shown in Fig. 14(a), along with the corresponding distribution for W + 2 jet events (Fig. 14(b)). The "hole" in the distribution in the lower left corner is caused by the loose kinematic cuts. There is good agreement between data and Monte Carlo. The projections of these variables are shown in Fig. 15, where the agreement between data and Monte Carlo is even more apparent. Figures 16(a)-(c) show the invariant mass of the two highest E_T jets (M_{jj}), the azimuthal difference between these jets ($\Delta\phi_{jj}$), and the difference in pseudorapidity between them ($\Delta\eta_{jj}$), respectively. There is good agreement with the W + 2 jets Monte Carlo prediction. Other distributions including the jet E_T spectra and the angle between electron and jets also show good agreement

with the W + 2 jet Monte Carlo calculation. This good agreement indicates that the final sample is composed primarily of W + jet events. To place an upper limit on the fraction of observed events that can be attributed to top quark production, we will compare the observed transverse mass distribution to that expected from W boson and top quark production.

IX. TRANSVERSE MASS

The transverse mass is a quantity well suited for distinguishing between W + jet production and t quark production, if the top quark mass is below the threshold for the decay $t \rightarrow Wb$, where the W in the final state is real (as opposed to virtual).[21] In particular, if the top mass is below the mass of the W, the distribution of $M_T^{e\nu}$ will be significantly softer for top events than for W events (see Fig. 17). We place an upper limit on the rate of top quark production by comparing the shapes of the transverse mass distributions measured in the electron + 2 jet data with those expected from top and W + jet production.

A. Measuring and modeling transverse mass

We have verified our ability to measure and model the transverse mass in electron + 2 jet events by studying inclusive electron events, Z^0 events, and the electron + 1 jet sample. Events with an electron and exactly one jet (with $E_T^{jet} > 10\ GeV$) provide a good testing ground for transverse mass measurements. Whereas the electron + 2 jet sample is possibly a mixture of $W^{\pm}$ and top events, it is expected that the electron + 1 jet events are dominated by W + 1 jet production (the maximum contribution from top quark events is less than 15%, which occurs for $M_{top} \sim 60$ GeV/c^2). The jet requirement implies that there is significant hadronic energy in these events, providing a non-trivial test of the transverse mass measurement.

A potential problem in the electron + 1 jet sample is the amount of background from dijet events, where one jet fakes an electron. To reduce this background, we impose a strict electron isolation cut, requiring

$$I = \frac{E_T^{cone} - E_T^{em}}{E_T^{cone}} < 0.1, \tag{24}$$

where E_T^{cone} is the transverse energy in a cone with radius $\Delta R = 0.7$ about the electron. There are 433 events that survive this cut (using the tight kinematic cuts, see Sec. VIII A). To further reduce the background from dijet events an explicit cut on the presence of a jet opposite the electron is made. Specifically, the event is rejected if there is a jet present such that

$$E_T^{jet} > 5 \text{ GeV} \quad \text{and} \quad 165^\circ < \Delta\phi_{ej} < 195^\circ, \tag{25}$$

where $\Delta\phi_{ej}$ is the azimuthal angle between the electron and jet vectors. The transverse mass distribution of the 333 events passing this dijet cut is shown in Fig. 18(a), along with the W + 1 jet distribution from the PAPAGENO Monte Carlo calculation employing the full detector simulation. The agreement between the electron + 1 jet data and the W + 1 jet calculation is excellent.

To further test the measurement of $M_T^{e\nu}$, we select a subset of the electron + 1 jet events, in which the Monte Carlo calculation predicts more smearing in $\not\!\!E_T$. We select events that satisfy any of the following:

$$\begin{aligned} &E_T^{jet} > 20 \ GeV, \\ &15^\circ < \Delta\phi_{ej} < 60^\circ, \text{ or} \\ &120^\circ < \Delta\phi_{ej} < 165^\circ. \end{aligned} \tag{26}$$

The Monte Carlo calculation indicates that the transverse mass resolution for these events is within 15% of the $M_T^{e\nu}$ resolution for W + 2 jet events. The transverse mass

distribution of this subset of the electron + 1 jet sample (consisting of 180 events) is shown in Fig. 18(b). Again the agreement between data and Monte Carlo is very good, and we conclude that the transverse mass in the electron + 2 jet sample is well modeled by the detector simulation.

B. Fitting transverse mass

We determine an upper limit on the production of $t\bar{t}$ pairs by fitting the transverse mass distribution of the electron + 2 jet sample to the theoretically predicted distributions for top quarks and for $W^{\pm}$ bosons. We assume that the electron + 2 jet data sample contains only $W^{\pm}$ and top events so that the $M_T^{e\nu}$ distribution of the observed events is given by

$$\frac{dN}{dM_T^{e\nu}} = \alpha T(M_T^{e\nu}) + \beta W(M_T^{e\nu}) \tag{27}$$

where $T(M_T^{e\nu})$ and $W(M_T^{e\nu})$ are the theoretical $M_T^{e\nu}$ distributions for $W^{\pm}$ and top, respectively, and the coefficients α and β are determined by the fit. The function $T(M_T^{e\nu})$ varies as a function of top mass and the fitting procedure is performed for each top mass investigated. As discussed previously, the ISAJET and PAPAGENO Monte Carlo programs plus the full detector simulation were used to determine the functions $T(M_T^{e\nu})$ and $W(M_T^{e\nu})$. For fitting purposes these functions have been normalized to the integrated luminosity of the real data (4.4 pb^{-1}). This way the coefficients α and β can be easily interpreted as the fraction of the predicted amount of top and $W^{\pm}$ in the data. Specifically, if top quarks and W bosons were present in the data with the rates predicted by the theoretical calculations, α and β will both be equal to one. We emphasize that we are not relying on the predicted rate of $W^{\pm}$ + 2 jet events, but only on the shape of the $M_T^{e\nu}$ distribution of these events. We discuss below the consequences of ignoring contributions other than top quark and $W^{\pm}$ events to the electron + 2 jet sample.

1. Effect of other backgrounds

As discussed previously, the electron + 2 jet sample contains known contributions from sources other than W + jet production. Besides backgrounds from b and c quark production and QCD sources, W production with $W \rightarrow \tau\overline{\nu_\tau} \rightarrow e\overline{\nu_e}\nu_\tau\overline{\nu_\tau}$ is expected to contribute. We have not attempted to model these contributions to the $M_T^{e\nu}$ distribution. In addition, if $M_{top} \lesssim 65$ GeV/c^2, there will be some contribution of t quarks from the decay $W \rightarrow t\bar{b}$. Because the rate for this process is low relative to the $t\bar{t}$ rate, we neglect this source of top quarks. Since all of these sources produce events at low values of transverse mass where only top events are expected to contribute, the fitted fraction of $t\bar{t}$ events will tend to increase. Thus this method of ignoring backgrounds results in a conservative estimate of the fraction of events attributed to $t\bar{t}$ production.

2. Fitting method

The fit used is a binned maximum likelihood method, with the contents of the bins treated with Poisson statistics.[22] Let k_i be the number of events observed in the i^{th} $M_T^{e\nu}$ bin and let m_i be the number of predicted events in the bin. The probability associated with the i^{th} bin is

$$P_i(k_i, m_i) = \frac{m_i^{k_i} e^{-m_i}}{k_i!}. \tag{28}$$

The total probability is then the product of the individual probabilities for each bin

$$\begin{aligned} P &= \prod_{i=1}^{N} P_i(k_i, m_i) \\ &= \prod_{i=1}^{N} \left(\frac{m_i^{k_i}}{k_i!} \right) e^{-m_i}, \end{aligned} \tag{29}$$

where N is the total number of bins in the fit. It is more convenient to maximize the logarithm of the likelihood,

$$\ln P = \sum_i (-\ln k_i! + k_i \ln m_i - m_i) . \qquad (30)$$

The dependence on α and β in Eq. (30) is contained in the m_i. We therefore may ignore the first term in this equation for the purposes of maximizing $\ln P$ with respect to α and β. The quantity maximized by the fitting routine is then given by

$$\ln P = \sum_i (k_i \ln m_i - m_i) . \qquad (31)$$

The program MINUIT[23] was used to maximize this expression.

We fit the transverse mass distributed in 8 GeV/c^2 bins over the range 24–120 GeV/c^2. We exclude the lowest bins of transverse mass to help minimize the non-W backgrounds discussed above. Few top or W events are expected with very low transverse mass values, especially once the kinematic cuts have been applied. Additionally, the coefficients α and β are constrained to be greater than zero on physical grounds, using a procedure advocated by the Particle Data Group.[24]

3. Fit results

The results of the fits are presented in Table IX. The fits are in good agreement with the data. The binned χ^2 is shown as an indication of the quality of fit. The statistical uncertainties shown correspond to a change in the log-likelihood of 1/2 unit. Correlations between α and β have been accounted for in the estimation of the uncertainties. Contour plots of α vs β are shown in Fig. 19 for two values of top mass. The small fitted values of α indicate an absence of top in the data, while the values of β obtained are within the theoretical uncertainties of the predicted W + jet cross sections, which are estimated to be 30–50%.[25]

To translate these fit values into a limit on the top mass, one must take into account systematic uncertainties.

X. SYSTEMATIC UNCERTAINTIES

We divide the systematic uncertainties into two groups. The first group consists of those effects that can affect both the shape of the $M_T^{e\nu}$ distribution as well as the number of events accepted. An investigation of the effect of these uncertainties on the top mass limit requires refitting the $M_T^{e\nu}$ distribution for each variation of the uncertain quantity. The systematic uncertainty associated with these effects is denoted $\Delta\alpha$. The second group of systematic uncertainties contains those effects that have been determined to affect only the rate of accepted events and not the shape of the $M_T^{e\nu}$ distributions. These effects contribute to an uncertainty in the overall normalization. The systematic uncertainty due to these effects is expressed fractionally and is denoted Δn.

A. Systematic uncertainties affecting transverse mass

The uncertainties for which refitting of the $M_T^{e\nu}$ distribution is necessary are

- the uncertainty in the jet energy scale in the Monte Carlo calculation,
- the uncertainty in the model of the underlying event, and
- the $M_T^{e\nu}$ interval over which the fit is performed.

Other possible sources of uncertainty, such as the electron energy calibration, the model for top quark production and decay, or the background contamination in the sample, have been studied and found to be negligible.

The estimated uncertainty on the Monte Carlo jet energy scale is $\pm 20\%$ (see Sec. VII C). The underlying event E_T is defined as the vector E_T of all energy that is not contained in either the electron cluster or in jet clusters with at least 5 GeV of observed transverse energy. A comparison of the underlying event E_T in electron + 2 jet events was made for real data, the W + 2 jet Monte Carlo events, and ISAJET

$t\bar{t}$ events. The mean E_T's of the underlying event agree to within 15% for the three samples; conservatively, we take the uncertainty in the underlying event E_T to be $\pm 20\%$.

We estimated the uncertainty in α by varying the scale (jet energy or underlying event energy) by the amounts stated above, recalculating the theoretical functions $T(M_T^{e\nu})$ and $W(M_T^{e\nu})$ and then refitting the $M_T^{e\nu}$ distributions. For example, if the jet energy scale is being varied, all jets in the event are multiplied by the appropriate factor (e.g., 1.2). The $\not\!\!E_T$ is recalculated and the jet cuts and the kinematic cuts are applied using the new jet energies and $\not\!\!E_T$. The transverse mass is then recalculated for events passing the cuts. In this way, changes in both acceptance and transverse mass are taken into account when determining the new $M_T^{e\nu}$ distributions, $T(M_T^{e\nu})$ and $W(M_T^{e\nu})$.

Table X shows the values of α obtained by refitting the transverse mass after making the variations in scale described above. This table also shows the effect of the particular choice of $M_T^{e\nu}$ interval over which the fit is performed. This is estimated by refitting over the intervals 16–120 GeV/c^2 and 32–120 GeV/c^2. The nominal fit results are also provided for comparison.

We take the average shift in the fitted value of α when we include a variation in one of the above effects as an estimate of the systematic uncertainty in α due to that effect. The 70 and 80 GeV/c^2 cases show no shift in the best value of α. The fit would prefer a value of α less than zero (by about 1/2 standard deviation), but α is constrained by the fit to be greater than zero. For the 80 GeV/c^2 case we consider the shift in the statistical error to estimate the uncertainty (using the rules described above). For the 70 GeV/c^2 case we have also fit the data allowing α to be less than zero and considering the shift in the best value of α obtained. The results of that fit are shown in Table XI. The contributions to $\Delta\alpha$ from each of the three systematic

effects discussed above are added in quadrature to form the results shown in Table XII. As discussed above, these values of $\Delta\alpha$ are derived only from the effects for which it was necessary to refit the $M_T^{e\nu}$ distribution. Additional systematic uncertainties in the overall normalization (Δn) are treated below.

The variations in the jet energy scale, the underlying event energy, and the $M_T^{e\nu}$ interval used in the fit described above should adequately account for any systematic uncertainties in the shape of the W + 2 jet transverse mass distribution. However, as an independent check we estimate the systematic uncertainties due to these effects by directly modifying the transverse mass distribution of the W + 2 jet events. If the function $W(M_T^{e\nu})$ is too wide then there will be more $W^{\pm}$ events allowed at low $M_T^{e\nu}$, thereby reducing the amount of top needed in the fit. We artificially narrowed the $W(M_T^{e\nu})$ distribution and then refit to the data. The degree of narrowing was determined by fitting the transverse mass of the electron + 1 jet data transverse mass distribution to the W + 1 jet PAPAGENO prediction. A reduction in width of the electron + 1 jet $M_T^{e\nu}$ distribution of 3% corresponded to a change in the log-likelihood of 1/2 unit in the fit to the W + 1 jet sample. This change in width was then applied to the W + 2 jet Monte Carlo sample and the resulting $M_T^{e\nu}$ distribution was fit to the $t\bar{t}$ Monte Carlo sample (M_{top} = 80 GeV/c^2) using the tight cuts. The result of this fit

$$\alpha = 0.074^{+.367}_{-.074} \tag{32}$$

(*cf.* nominal $0.00^{+0.27}_{-0.00}$) shows the variation in α to be within the range of the systematic uncertainty given above (Table XII).

B. Systematic uncertainties in normalization

The second category of systematic effects do not require refitting the transverse mass distributions. These effects, which may modify the acceptance in detecting $t\bar{t}$

or $W^{\pm}$ events, are

- the production properties of the top quark,
- the model of the fragmentation of a top quark into a hadron,
- the number of jets from initial state radiation,
- the modeling of the electron detection efficiency, and
- the integrated luminosity.

We have studied possible variations in $t\bar{t}$ production properties by comparing the ISAJET and PAPAGENO Monte Carlo calculations for $t\bar{t}$ production. The $t\bar{t}$ events produced by these different calculations are quite similar, the only significant difference being the softer p_T spectrum for top quarks in the PAPAGENO calculation, especially at low values of M_{top}. This difference in t quark p_T has no significant effect on the $M_T^{e\nu}$ distribution, given the kinematic cuts. The fitted value of α using the PAPAGENO $t\bar{t}$ transverse distribution for M_{top}=40 GeV/c^2 (the top mass for which there is the biggest discrepancy between PAPAGENO and ISAJET) does not differ significantly from the nominal fit result. However, this discrepancy does lead to a decrease in the $t\bar{t}$ acceptance for $M_{top} \lesssim 50$ GeV/c^2, for which we add a systematic uncertainty in the acceptance, shown in Table XIII. For $M_{top} \geq 60$ GeV/c^2 the two calculations are in good agreement.

To model the fragmentation of partons, ISAJET uses the Peterson parametrization[26] of the fragmentation function, which is consistent with b and c quark data:

$$D_Q^H(z) = \frac{N}{z\left[1-(1/z)-\frac{\epsilon}{1-z}\right]^2}, \tag{33}$$

where $D_Q^H(z)$ is the probability that a heavy quark Q will form a hadron H with momentum fraction $z = p_H/p_Q$, ϵ is a parameter proportional to $1/M_Q^2$, and N is

a normalization constant. To investigate the effect of a systematic uncertainty in the fragmentation model, we have varied ϵ in Eq. (33) from $0.2/M_{top}^2$ to $1.5/M_{top}^2$ (ISAJET's default value is $\epsilon = 0.5/M_{top}^2$). The only significant effect is on the isolation properties of electrons. The larger value of ϵ leads to a decrease in electron efficiency of 18% and 5% for 40 GeV/c^2 and 70 GeV/c^2, respectively. The shape of the $M_T^{e\nu}$ distribution is not significantly affected. The fractional decrease in $t\bar{t}$ acceptance is taken as the systematic uncertainty due to t quark fragmentation.

The acceptance of $t\bar{t}$ events is sensitive to the number of jets arising from initial state radiation, and we therefore include as a systematic uncertainty the effect on the $t\bar{t}$ acceptance of varying the amount of initial state radiation. This change in acceptance was calculated by reselecting the $t\bar{t}$ Monte Carlo events with the additional requirement that all jets come from t quark (or $\bar{t}$ quark) decays. We then take half of this change as the fractional uncertainty in the $t\bar{t}$ acceptance due to uncertainty in the initial state radiation.

The uncertainty in the measured electron efficiency as compared to that reproduced by the Monte Carlo has been estimated to be $\pm 5\%$. This uncertainty covers the range of measured efficiencies determined from W and Z boson decays in the data. The integrated luminosity for the data sample of 4.4 pb^{-1} has an uncertainty of $\pm 15\%$. A summary of these uncertainties as a function of top mass is presented in Table XIII.

When considering top quark masses below 40 GeV/c^2, we have found that the systematic uncertainties grow rapidly, particularly those due to initial state radiation and to top quark fragmentation. The uncertainty in the p_T of the produced top quark also grows as the top quark mass decreases. Furthermore, the efficiency for detecting top quarks is falling rapidly in this mass region. For these reasons, we will not attempt to exclude the region $M_{top} < 40$ GeV/c^2. The mass region below 40 GeV/c^2 is safely excluded by other searches.[9,8]

XI. TOP MASS LIMIT

The fit results presented in Table IX show no evidence for top quark production. Using these fit results we set an upper bound on the $t\bar{t}$ production cross section, which is a function of M_{top}. We then compare these upper limits with the theoretically predicted $t\bar{t}$ production cross section to establish limits on the top quark mass.

We calculate the upper limit on the top cross section using the fitted value of α and its statistical and systematic uncertainties. We eliminate the necessity for making assumptions about the nature of the likelihood distribution for these fits by working with the full likelihood function. This is obtained by exponentiating and normalizing the log-likelihood function, which is determined by maximizing the value of the log-likelihood as a function of β for each value of α. Figure 20 shows this likelihood function for the 60 and 80 GeV/c^2 fits. The 95% confidence level (C.L.) upper limit on α is calculated by integrating this function after smearing it appropriately by the systematic uncertainty.

The systematic uncertainty has been divided into two parts as described above (Sec. X). To see why this is necessary one must examine in more depth the meaning of the coefficient α. This coefficient has been defined as the fraction of the predicted $t\bar{t}$ cross section that is needed to fit the data. Then α may be written as

$$\alpha = \frac{n_{\rm obs}}{n_{t\bar{t}}} = \frac{n_{\rm obs}}{\epsilon \sigma_{t\bar{t}} \int \mathcal{L}\, dt} \tag{34}$$

where $n_{\rm obs}$ is the number of $t\bar{t}$ events needed to fit the data, $n_{t\bar{t}}$ is the number of $t\bar{t}$ events expected in the final sample, ϵ is the efficiency for detecting $t\bar{t}$ events, $\sigma_{t\bar{t}}$ is the $t\bar{t}$ production cross section used in the Monte Carlo calculation, and $\int \mathcal{L}\, dt$ is the integrated luminosity. The numerator in this expression depends only on the $M_T^{e\nu}$ distribution of the data and on the shapes of the Monte Carlo distributions. The portion of the systematic uncertainty that requires refitting the $M_T^{e\nu}$ distribution,

called $\Delta\alpha$ above, is the systematic uncertainty associated with n_{obs}. This uncertainty must be expressed not as a fractional uncertainty in α (or n_{obs}), but as an absolute uncertainty in the magnitude of α (or n_{obs}). To see that this is true, one may consider the case when the fit gives α=0. Considering $\Delta\alpha$ as a fractional uncertainty would result in zero uncertainty in the number of $t\bar{t}$ events in the fit, a clearly erroneous result. The uncertainty in the overall normalization, Δn, derives from uncertainties in ϵ, the efficiency for detecting $t\bar{t}$ events, and in $\int \mathcal{L}\, dt$, the integrated luminosity.

The probability distribution is smeared according to its systematic uncertainty using a simple Monte Carlo program. First, a value of α, called α_0, is generated from the parent probability distribution obtained from the likelihood function. Then the smearing due to $\Delta\alpha$ is applied by adding to α_0 a random number, whose parent distribution is Gaussian with mean zero and standard deviation $\Delta\alpha$. Then the smearing due to Δn is applied by multiplying by a number whose parent distribution is Gaussian with mean one and standard deviation Δn. This procedure is repeated one million times, yielding the smeared probability function for a given top mass, examples of which are shown in Fig. 21. This function is then integrated over the range $0 < \alpha < \infty$ and normalized to unity. The normalized function is used to determine the value of α, denoted α_{max}, above which we find 5% of the area under the probability curve. This is the 95% C.L. upper limit for α. The 95% C.L. upper limit on the $t\bar{t}$ cross section derived from the fit is then

$$\sigma_{max} = \sigma_{t\bar{t}}\, \alpha_{max}. \tag{35}$$

We emphasize that this upper limit on the cross section is independent of any theoretical prediction of the $t\bar{t}$ production cross section. This procedure is repeated for each value of M_{top}, yielding an upper limit on the $t\bar{t}$ cross section as a function of t quark mass. Table XIV summarizes this calculation.

Figure 22 shows the upper limit on the observed top quark cross section as a function of top mass. The two solid curves are produced by performing the analysis with the loose and tight kinematic cuts. The region above these curves is excluded at 95% C.L. We compare these curves with the calculation of the $t\bar{t}$ production cross section by Altarelli *et al.*[7] This calculation is based on the QCD total cross section formulas for heavy quark production, complete through order α_s^3, by Nason *et al.*[18] The shaded region represents the theoretical uncertainty in the calculation based on various choices of the renormalization scale, μ,and the QCD scale parameter, Λ_s. The points of intersection of the solid curve with the lower edge of the shaded band show that the top quark is excluded at 95% C.L. for

$$40 < M_{top} < 77 \text{ GeV/c}^2. \tag{36}$$

The systematic uncertainties on jet detection efficiency and top fragmentation grow rapidly with decreasing M_{top}, so we do not extend the lower mass limit below 40 GeV/c^2.

XII. CONCLUSIONS

Based on an analysis of events with a high-p_T electron, significant $\not\!\!E_T$, and two or more jets with $E_T > 10$ GeV, we have determined an upper limit on the standard model $t\bar{t}$ production cross section, and exclude at 95% confidence level the existence of a standard model top quark in the range $40 < M_{top} < 77$ GeV/c^2. This mass limit is based on the reaction $\bar{p}p \rightarrow t\bar{t}+X$ and therefore depends on the theoretical prediction of the cross section for this process. The analysis also depends on the standard model prediction for the semi-leptonic branching ratio of 1/9 for the top quark. Given these assumptions, the 77 GeV/c^2 limit is the strongest limit on the top quark mass to date. However, there exist weaker limits from e^+e^- colliders ($M_{top} \gtrsim 45$ GeV/c^2) that are not subject to these theoretical assumptions.

Because the top quark mass enters into radiative corrections for various electroweak quantities (e.g.. M_Z, $\sin^2\theta_W$), the top mass can be estimated from measurements of a number of independent quantities.[11] Figure 23, taken from a recent paper by Langacker,[27] shows the dependence of $\sin^2\theta_W$ on M_{top}, based on these measurements. These data include measurements of W and Z^0 boson masses, atomic parity violation, and neutrino scattering (some of the data have been omitted from the figure for the sake of clarity). Also shown is our direct limit of $M_{top} > 77$ GeV/c^2 at 95% CL. A fit to the data yields a top mass of 143^{+37}_{-44} GeV/c^2, for a Higgs boson mass of $M_H = 100$ GeV/c^2. Although the uncertainty in the predicted top quark mass is large due to the unknown Higgs mass, the results of these fits to electroweak data are consistent with the CDF top quark mass limit.

XIII. ACKNOWLEDGEMENTS

We thank the staff of the Fermilab Accelerator Division and the CDF technical and support staff. We acknowledge International Business Machines Corporation for the 3090 supercomputer CPU time it made available to perform several of the Monte Carlo calculations. This work was supported by the Department of Energy, the National Science Foundation, Istituto Nazionale di Fisica Nucleare, the Ministry of Science, Culture and Education of Japan, and the A. P. Sloan Foundation.

[1]G. L. Kane and M. Peskin, Nucl. Phys. **B195**, 29 (1985);
A. Bean *et al.*, Phys. Rev. **D35**, 3533 (1987).

[2]W. Bartel *et al.*, JADE collab., Phys. Lett. **146B**, 437 (1984).

[3]H. Albrecht *et al.*, Argus collab., Phys. Lett. **192B**, 245 (1987).
M. Artuso *et al.*, CLEO collab., Phys. Rev. Lett. **62**, 2233 (1989).

[4]F. Abe *et al.*, CDF collab., Phys. Rev. Lett. **64**, 142 (1990).

[5]T. Kamae, Proceedings of the XXIV International Conference on High Energy Physics, edited by R. Kotthaus and J. Kuhn, Springer-Verlag (1989), p. 156.

[6]C. Albajar *et al.*, UA1 collab., Z. Phys. **C37** 505, (1984);
I. J. Kroll, Proceedings of the XXIV International Conference on High Energy Physics, edited by R. Kotthaus and J. Kuhn, Springer-Verlag (1989), p. 1416.

[7]G. Altarelli, M. Diemoz, G. Martinelli and P. Nason, Nucl. Phys. **B308**, 724 (1988).

[8]F. Abe *et al.*, CDF collab., Phys. Rev. Lett. **64**, 147 (1990).

[9]D. Decamp *et al.*, ALEPH collab., CERN-EP/89-165 (1989). The limit quoted in this paper is $M_{top} > 45.8$ GeV/c^2;
M. Akrawy *et al.*, OPAL collab., CERN-EP/89-154 (1989).

[10]T. Åkesson *et al.*, UA2 collab., CERN-EP/89-152 (1989).

[11]U. Amaldi *et al.*, Phys. Rev. **D36**, 1385 (1987).

[12]P. Langacker, Phys. Rev. Lett. **63**, 1920 (1989).

[13]S. Glashow and E. Jenkins, Phys. Lett. **196B**, 233 (1987).

[14]F. Abe *et al.*, CDF collab., Phys. Rev. Lett. **64**, 152 (1990).

[15]F. Abe *et al.*, CDF collab., Nucl. Instr. Meth. **A271**, 387 (1988).

[16]F. Abe *et al.*, CDF collab., Phys. Rev. Lett. **62**, 3020 (1989).

[17]F. Paige and S. D. Protopopescu, BNL Report No. BNL 38034, 1986 (unpublished). The $b\bar{b}$ and $t\bar{t}$ event samples were generated with version 6.10 and 6.21, respectively.

[18]P. Nason, S. Dawson and R. K. Ellis, Nucl. Phys. **B303**, 607 (1988).

[19]I. Hinchliffe, in preparation. Version 2.71 of PAPAGENO was used for the W + jets calculations.

[20]R. K. Ellis and R. J. Gonsalves, Proceedings of the Supercollider Physics Topical Conference, edited by D. Soper, World Scientific (1985), p. 287.

[21]J. Rosner, Phys. Rev. **D39**, 3297 (1989).
J. Rosner, Phys. Rev. **D40**, 1701 (1989).
H. Baer, V. Barger, and R. J. N. Phillips, Phys. Lett. **B221**, 398 (1989).

[22]F. Solmitz, Ann. Rev. Nucl. Sci. **14**, 375 (1964).

[23]F. E. James and M. Roos, Comput. Phys. Commun. **10**, 343 (1975).

[24]The Particle Data Group, G.P. Yost *et al*, Phys. Lett. **B204**, 74 (1988).

[25]M. Mangano and S. Parke, Phys. Rev. **D41**, 59 (1990).

[26]C. Peterson, D. Schlatter, I. Schmidt and P. Z. Zerwas, Phys. Rev. **D27**, 105 (1983).

[27]P. Langacker, Univ. of Pennsylvania preprint UPR-0421T, 1990 (to be published in the Review of Particle Properties, 1990).

TABLE I. Cuts used in the electron selection.

Variable	Cut
E_T^{em}	> 15 GeV
had/em	< 0.05
$\mathcal{L}_{shr}$	< 0.2
χ^2_Z	< 10
χ^2_ϕ	< 10
Δz	< 3 cm
Δx	< 1.5 cm
E/p	< 1.5

TABLE II. Summary of conversion analysis for inclusive electrons.

Electron candidates	16598
Conversions candidates removed	5323
w/ $f_{VTPC} < 0.2$	1604
w/ $f_{VTPC} > 0.2$	3719
Number of conversions passing both cuts	1310
Number of like-sign candidates removed	1512
Conversion removal efficiency, ϵ_{conv}	0.880 ± 0.038
Conversions as fraction of final sample, f_{bg}	0.050 ± 0.015
Fraction of prompt electrons removed, f_{prompt}	0.101 ± 0.004

TABLE III. Summary of electron efficiency analysis. The uncertainties shown are statistical only.

Overall Efficiency		
	Data	Monte Carlo
N_Z	109	374
N_2	68	229
ϵ	$.768 \pm .032$	$.760 \pm .017$

Single Cut Efficiencies				
Cut	N_c	ϵ_c	N_c	ϵ_c
had/em	104	.972	364	.983
E/p	93	.910	355	.969
$\mathcal{L}_{shr}$	105	.977	342	.947
Δx	105	.977	366	.987
Δz	107	.989	355	.969
χ^2_ϕ	84	.859	284	.851
χ^2_Z	100	.949	348	.957

TABLE IV. Summary of the calculation of the charged pion background in the inclusive electron sample.

Charged pion background calculation		
Electron efficiency	ϵ_e	$0.95 \pm .02$
Pion efficiency	ϵ_π	$0.57 \pm .10$
Inclusive electron candidates	N_p	11157
Events failing *had/em* cut only	N_f	2152
Number of real electrons	N_e	9397 ± 1100
Number of real pions	N_π	3912 ± 1100
Background as % of sample	$f_{bg}^{\pm}$	20 ± 10

TABLE V. Efficiency of kinematic cuts as a function of M_{top}. The table lists the fraction of the electron + 2 jet events from $t\bar{t}$ production that survive the loose and tight selection (see text) as a function of M_{top}.

M_{top} (GeV/c^2)	Loose Cuts	Tight Cuts
40	0.25 ± 0.02	0.13 ± 0.02
50	0.49 ± 0.03	0.25 ± 0.03
60	0.63 ± 0.03	0.37 ± 0.03
70	0.73 ± 0.03	0.47 ± 0.03
75	0.75 ± 0.02	0.55 ± 0.02
80	0.79 ± 0.02	0.59 ± 0.03

TABLE VI. Summary of the calculation of the non-isolated electron background in the electron + 2 jet sample.

		Loose Cuts	Tight Cuts
Efficiency of E_T^{iso} cut for $W^{\pm}$ + jets	ϵ_W	$0.93 \pm .02$	
Efficiency of E_T^{iso} cut for non-isolated background	ϵ_b	$0.33 \pm .05$	
Electron + 2 jet candidates passing E_T^{iso} cut	N_p	123	104
Events failing E_T^{iso} cut only	N_f	65	33
Number of isolated electrons	N_W	102 ± 33	98 ± 28
Number of non-isolated electrons	N_b	86 ± 30	39 ± 26
Background as % of sample	f_{bg}^{non}	$23 \pm 9\%$	$12 \pm 8\%$

TABLE VII. Conversion efficiency and background as a function of electron E_T.

	$E_T^{em} > 12\ GeV$	$E_T^{em} > 15\ GeV$	$E_T^{em} > 20\ GeV$
ϵ_{conv}	$.860 \pm .033$	$.880 \pm .038$	$.900 \pm .055$
f_{prompt}	$.113 \pm .004$	$.101 \pm .004$	$.065 \pm .005$
f_{bg}	$.059 \pm .014$	$.050 \pm .015$	$.028 \pm .013$

TABLE VIII. Estimates of the size of the non-electron backgrounds in the for the final sample of electron + 2 jet events.

	Loose Cuts	Tight Cuts
$\pi^{\pm}$	$0 \pm 3\%$	$0 \pm 5\%$
$\gamma \rightarrow e^+e^-$	$4.4 \pm 1.3\%$	$2.6 \pm 1.3\%$
Total	$4.4 \pm 3\%$	$2.6 \pm 5\%$

TABLE IX. Transverse mass fit results. The loose cuts were used for $40 \leq M_{top} < 65$ GeV/c^2 and the tight cuts were used for the higher top masses. The uncertainties shown are statistical.

M_{top} GeV/c^2	α	β	χ^2 (10 dof)
40	0.07 ± 0.05	1.27 ± 0.14	9.7
50	0.06 ± 0.05	1.29 ± 0.14	10.4
60	0.11 ± 0.08	1.26 ± 0.15	10.4
70	$0.00^{+0.12}_{-0.00}$	1.28 ± 0.13	9.4
75	$0.00^{+0.18}_{-0.00}$	1.28 ± 0.13	9.4
80	$0.00^{+0.27}_{-0.00}$	1.28 ± 0.13	9.4

TABLE X. Systematic variation of fitted $t\bar{t}$ fraction α. The uncertainties shown are statistical only. The loose cuts have been used for $M_{top} < 65$ GeV/c^2, the tight cuts for the other masses.

M_{top} (GeV/c^2)	Nominal Fit	Jet Energy Scale		Underlying Event		Fit Interval (GeV/c^2)	
		+20%	−20%	+20%	−20%	16–120	32–120
40	$.07 \pm .05$	$.05 \pm .04$	$.05 \pm .07$	$.07 \pm .05$	$.07 \pm .07$	$.03 \pm .05$	$.07 \pm .05$
50	$.06 \pm .05$	$.06 \pm .05$	$.07 \pm .07$	$.05 \pm .05$	$.04 \pm .05$	$.05 \pm .05$	$.05 \pm .05$
60	$.11 \pm .08$	$.07 \pm .06$	$.13 \pm .11$	$.10 \pm .09$	$.11 \pm .08$	$.06 \pm .07$	$.09 \pm .08$
70	$.00 \pm .12$	$.00 \pm .08$	$.00 \pm .13$	$.00 \pm .12$	$.00 \pm .11$	$.00 \pm .09$	$.00 \pm .17$
75	$.00 \pm .17$	$.00 \pm .21$	$.00 \pm .18$	$.00 \pm .17$	$.00 \pm .18$	$.00 \pm .12$	$.00 \pm .26$
80	$.00 \pm .27$	$.00 \pm .33$	$.00 \pm .46$	$.00 \pm .21$	$.00 \pm .30$	$.00 \pm .22$	$.00 \pm .45$

TABLE XI. Systematic variations in α for M_{top} = 70 GeV/c^2. The fit coefficients α, and β are allowed to be negative for this fit.

Systematic Effect	$t\bar{t}$ fraction, α
Nominal	$-0.06 \pm .14$
Jet Scale +20%	$-0.15 \pm .16$
Jet Scale −20%	$-0.16 \pm .18$
Underlying Event +20%	$-0.08 \pm .17$
Underlying Event −20%	$-0.11 \pm .18$

TABLE XII. Uncertainties in α ($\Delta\alpha$) due to systematic effects for which the $M_T^{e\nu}$ distribution must be refit. The *Total* $\Delta\alpha$ column is the quadrature sum of the three effects.

M_{top} (GeV/c^2)	Jet Scale	Underlying Event	$M_T^{e\nu}$ Interval	Total $\Delta\alpha$
40	0.02	0.00	0.02	0.023
50	0.01	0.01	0.01	0.018
60	0.03	0.01	0.03	0.040
70	0.10	0.04	0.04	0.112
75	0.05	0.01	0.08	0.094
80	0.14	0.05	0.10	0.170

TABLE XIII. Systematic uncertainties in the overall normalization. Values are expressed as a fraction of the total $t\bar{t}$ acceptance. The uncertainties summed in quadrature are listed in the Δn column.

M_{top} GeV/c^2	Production Model	Fragmentation Model	Initial State Radiation	Electron Efficiency	Integrated Luminosity	Δn
40	0.18	0.130	0.210	0.05	0.15	0.34
50	0.15	0.103	0.170	0.05	0.15	0.29
60	–	0.076	0.125	0.05	0.15	0.22
70	–	0.050	0.090	0.05	0.15	0.19
75	–	0.050	0.070	0.05	0.15	0.18
80	–	0.050	0.045	0.05	0.15	0.17

TABLE XIV. Summary of the calculation of the upper limit on the $t\bar{t}$ production cross section. The theoretical prediction of Altarelli *et al.* ($\sigma_{t\bar{t}}$) and the lower bound on that calculation ($\sigma_{t\bar{t}}^{\min}$) are shown for comparison.

M_{top}					Theoretical	
(GeV/c^2)	$\alpha \pm$ (stat)	$\Delta\alpha$	Δn	$\sigma_{\max}$ (pb)	$\sigma_{t\bar{t}}$ (pb)	$\sigma_{t\bar{t}}^{\min}$ (pb)
40	0.07 ± 0.05	0.023	0.34	2410	9630	7130
50	0.06 ± 0.05	0.018	0.28	648	2930	2140
60	0.11 ± 0.08	0.040	0.22	408	1270	920
70	$0.00^{+0.12}_{-0.00}$	0.112	0.19	266	556	406
75	$0.00^{+0.18}_{-0.00}$	0.090	0.18	238	387	282
80	$0.00^{+0.27}_{-0.00}$	0.170	0.17	281	285	208

FIG. 1. Cross section for top quark production in $\bar{p}p$ collisions at $\sqrt{s} = 1.8$ TeV. The solid curve is for $t\bar{t}$ pair production and the dashed curve is for $W \rightarrow t\bar{b}$.

FIG. 2. Elevation view of one-half of the CDF detector. The detector is forward-backward symmetric.

FIG. 3. Distribution of variables used to select the inclusive electron sample: (a) E_T^{em}, (b) *had/em*, (c) χ^2_ϕ, and (d) χ^2_Z. The shaded areas are cut. For plots (a)–(c) all the cuts have been applied except for the one on the quantity being plotted. Plot (d) has all cuts applied.

FIG. 4. Distributions of variables used to select the inclusive electron sample: (a) Δx, (b) Δz, (c) $\mathcal{L}_{shr}$, and (d) E/p. The shaded areas are cut. For plots (a) and (d) all the cuts have been applied except for the one on the quantity being plotted. Plots (b) and (c) have all cuts applied.

FIG. 5. The distributions for the variables used to identify conversions: (a) the invariant mass of electron candidate with a nearby track, and (b) f_{VTPC}, the fraction of expected hits observed in the VTPC along the electron's trajectory. The candidates falling in the shaded regions are rejected.

FIG. 6. Scatterplot of $\not\!\!E_T$ vs E_T^{em} for the inclusive electron sample. Only half of the total sample is shown for clarity.

FIG. 7. The E_T distributions for the leading and non-leading jets ((a) and (b)) and for the electron candidates (c) are shown as the plotted points. The histograms are the Monte

Carlo predictions for b and c quark production.

FIG. 8. Isolation variable E_T^{iso} for electrons with $E_T^{em} < 20\ GeV$, for data (plotted points), $b\bar{b}$ Monte Carlo (solid curve), and $t\bar{t}$ ($M_{top} = 75\ GeV$, histogram). Residual $W^{\pm}$ and Drell-Yan events form the peak in the very lowest E_T^{iso} bin. The normalization of the Monte Carlo curves is discussed in the text.

FIG. 9. Mass spectrum of di-electron candidates. The shaded region is cut.

FIG. 10. Probability of finding a jet cluster with observed $E_T > 10$ GeV in the hemisphere opposite the photon for direct photon events. The horizontal axis is the photon p_T (assumed equal to the parton p_T). The solid curve is the Monte Carlo prediction.

FIG. 11. Monte Carlo distributions of the pseudorapidity of jets from top ($M_{top} =$ 75 GeV/c^2, solid curve) and W + 2 jet events (dashed curve).

FIG. 12. Scatterplot of $\not\!\!E_T$ vs E_T^{em} for events with an electron and two or more jets. Conversions and Z^0 events have been removed as described in the text. The plot for the data events is shown in (a) along with the contours for the tight and loose kinematic cuts. Plot (b) shows Monte Carlo $t\bar{t}$ events with $M_{top} = 70$ GeV/c^2, and plot (c) shows Monte Carlo W + 2 jet events. The integrated luminosities of the $t\bar{t}$ and W + jet samples are 13 pb^{-1} and 41 pb^{-1}, respectively.

FIG. 13. The $\not\!\!E_T$ vs E_T^{em} scatterplot for background events: (a) shows the distribution for conversion events and (b) shows it for non-isolated electrons ($E_T^{iso} > 2$ GeV).

FIG. 14. The scatterplot of $M_T^{e\nu}$ vs $p_T^{e\nu}$ for the electron + 2 jet data sample with the loose cuts is shown in (a). For comparison, we show the corresponding distribution for the W + 2 jet Monte Carlo events in (b).

FIG. 15. The $M_T^{e\nu}$ and $p_T^{e\nu}$ distributions for electron + 2 jet data with the loose cuts applied is shown in (a) and (b). The solid curves show the distributions for the Monte Carlo W + 2 jet events (normalized to the data), and the dashed curve shows the distributions for Monte Carlo $t\bar{t}$ events for $M_{top} = 60$ GeV/c^2 (normalized to the number of events predicted by the Altarelli cross section).

FIG. 16. Comparison of the electron + 2 jet data with the loose cuts applied (plotted points) with the W + 2 jet Monte Carlo predictions (solid curves): plot (a) shows the di-jet invariant mass distribution, plot (b) shows the distribution of the azimuthal difference between the two leading jets, and plot (c) shows the distribution of the pseudorapidity difference between the two leading jets.

FIG. 17. Monte Carlo distributions of $M_T^{e\nu}$ for top quarks with $M_{top} = 75$ GeV/c^2 (dashed curve) and W + 2 jet events (solid curve).

FIG. 18. Transverse mass distribution for electron + 1 jet events with the tight cuts applied. The full electron + 1 jet sample is shown in (a), and a subset of electron + 1 jet events where more $M_T^{e\nu}$ smearing is expected (as described in the text) is shown in (b).

FIG. 19. Fit contours in α–β space, as calculated by MINUIT. The contour for the fit to $M_{top} = 80$ GeV/c^2 is shown in (a), and for $M_{top} = 60$ GeV/c^2 in (b). The contours correspond to changes in the log-likelihood function of 0.5, 2.0, and 4.5. The constraint

$\alpha > 0$ has been imposed for the 80 GeV/c^2 fit.

FIG. 20. Normalized likelihood distributions for the 80 (solid curve) and 60 (dashed curve) GeV/c^2 fits.

FIG. 21. Smeared likelihood distributions for the 80 (solid curve) and 60 (dashed curve) GeV/c^2 fits.

FIG. 22. The 95% C.L. upper limit for the $t\bar{t}$ production cross section as a function of top mass is given by the solid curves. The shaded region gives the predicted $t\bar{t}$ cross section (see text). The plotted points show the $t\bar{t}$ efficiency as a function of M_{top} (right-hand scale).

FIG. 23. The $\pm 1\sigma$ uncertainties in $\sin^2\theta_W \equiv 1 - M_W^2/M_Z^2$, determined from M_Z (dashed line), M_W/M_Z (dotted line), and νN neutral current data (dash-dotted line) as a function of M_{top} for $M_H = 100$ GeV/c^2. Also shown is the direct lower limit from the nonobservation of the t quark in $\bar{p}p \rightarrow t\bar{t} + X$ (long-short line), and the region (solid line) in $\sin^2\theta_W$-M_{top} allowed by all data at 90% CL ($\Delta\chi^2 = 4.6$).

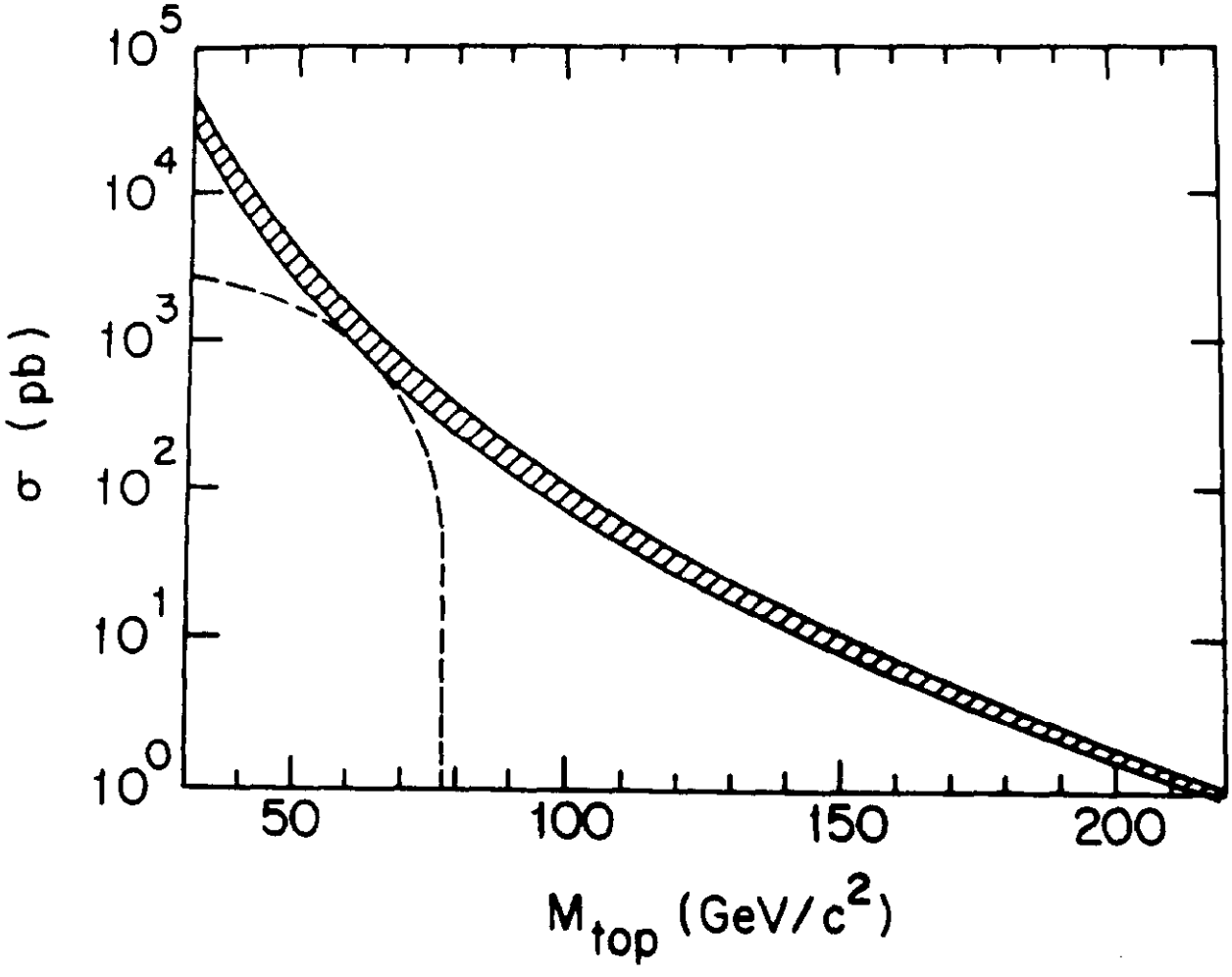

FIG. 1. Cross section for top quark production in $\bar{p}p$ collisions at $\sqrt{s} = 1.8$ TeV. The solid curve is for $t\bar{t}$ pair production and the dashed curve is for $W \rightarrow t\bar{b}$.

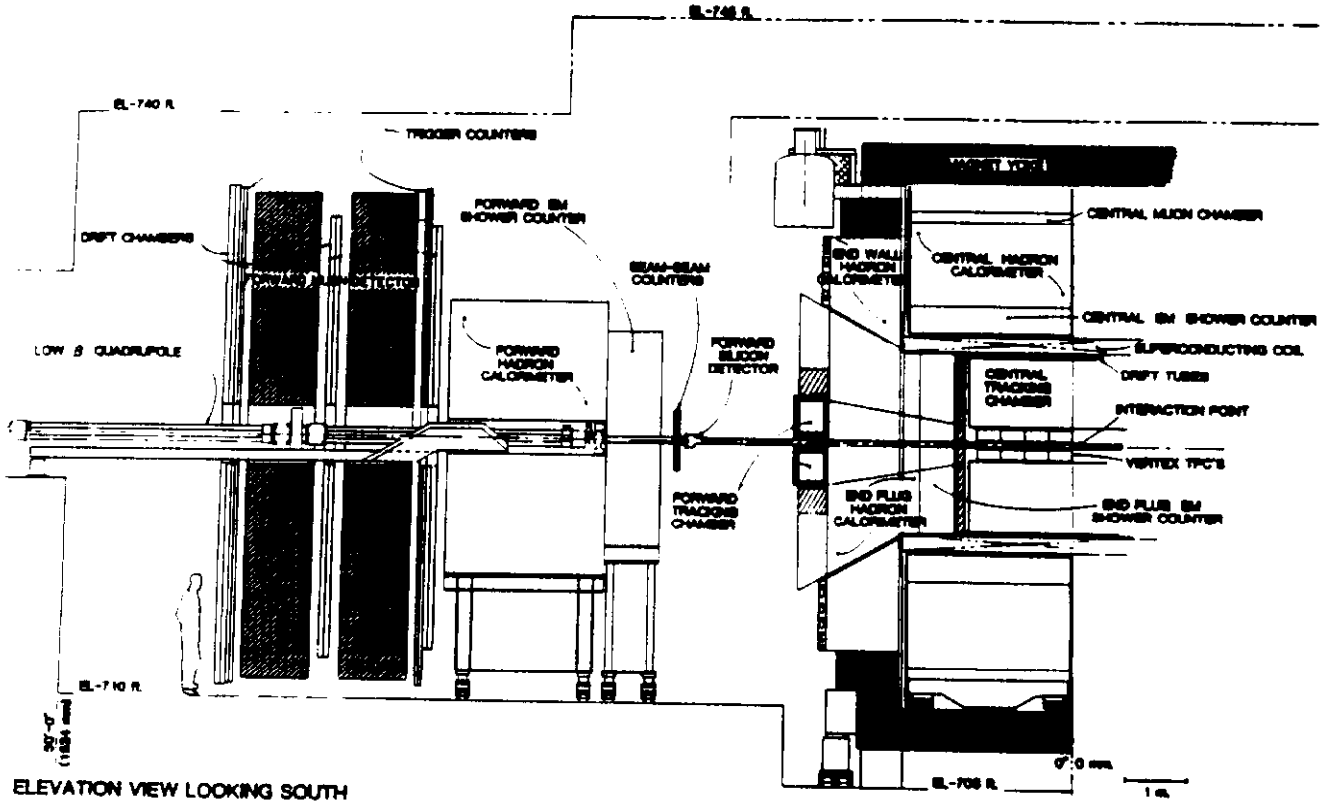

FIG. 2. Elevation view of one-half of the CDF detector. The detector is forward-backward symmetric.

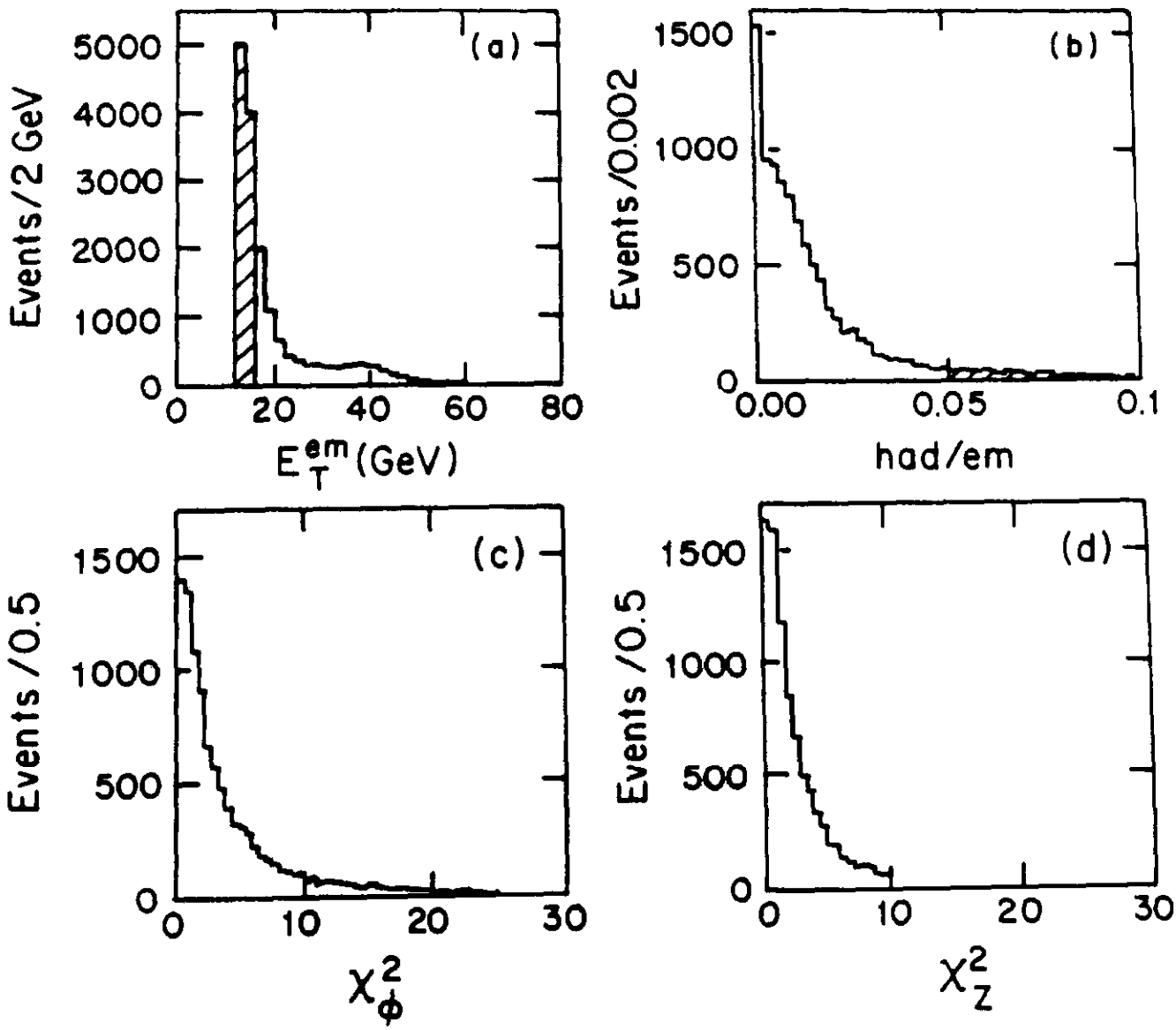

FIG. 3. Distribution of variables used to select the inclusive electron sample: (a) E_T^{em}, (b) *had/em*, (c) χ^2_ϕ, and (d) χ^2_Z. The shaded areas are cut. For plots (a)–(c) all the cuts have been applied except for the one on the quantity being plotted. Plot (d) has all cuts applied.

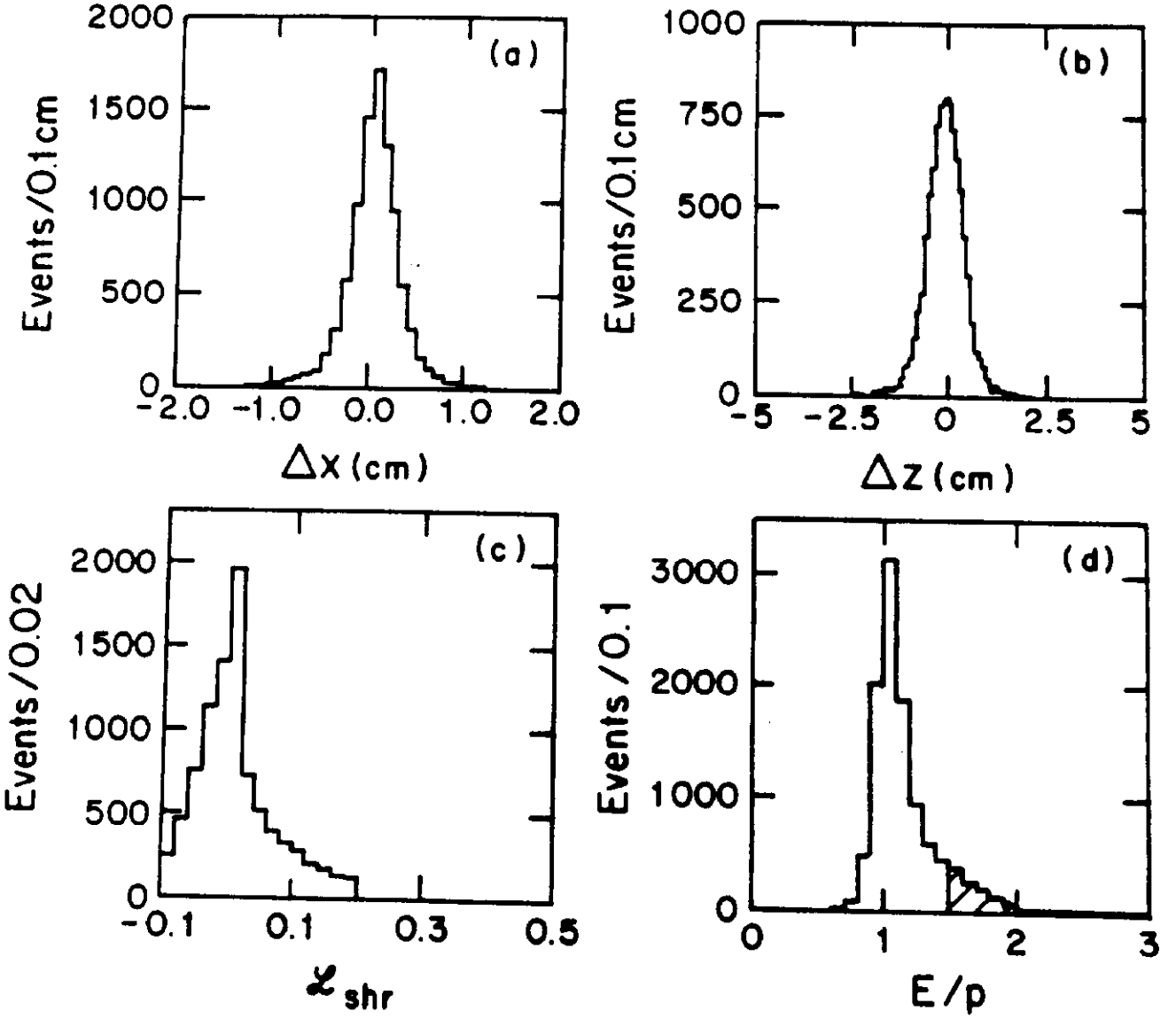

FIG. 4. Distributions of variables used to select the inclusive electron sample: (a) Δx, (b) Δz, (c) $\mathcal{L}_{shr}$, and (d) E/p. The shaded areas are cut. For plots (a) and (d) all the cuts have been applied except for the one on the quantity being plotted. Plots (b) and (c) have all cuts applied.

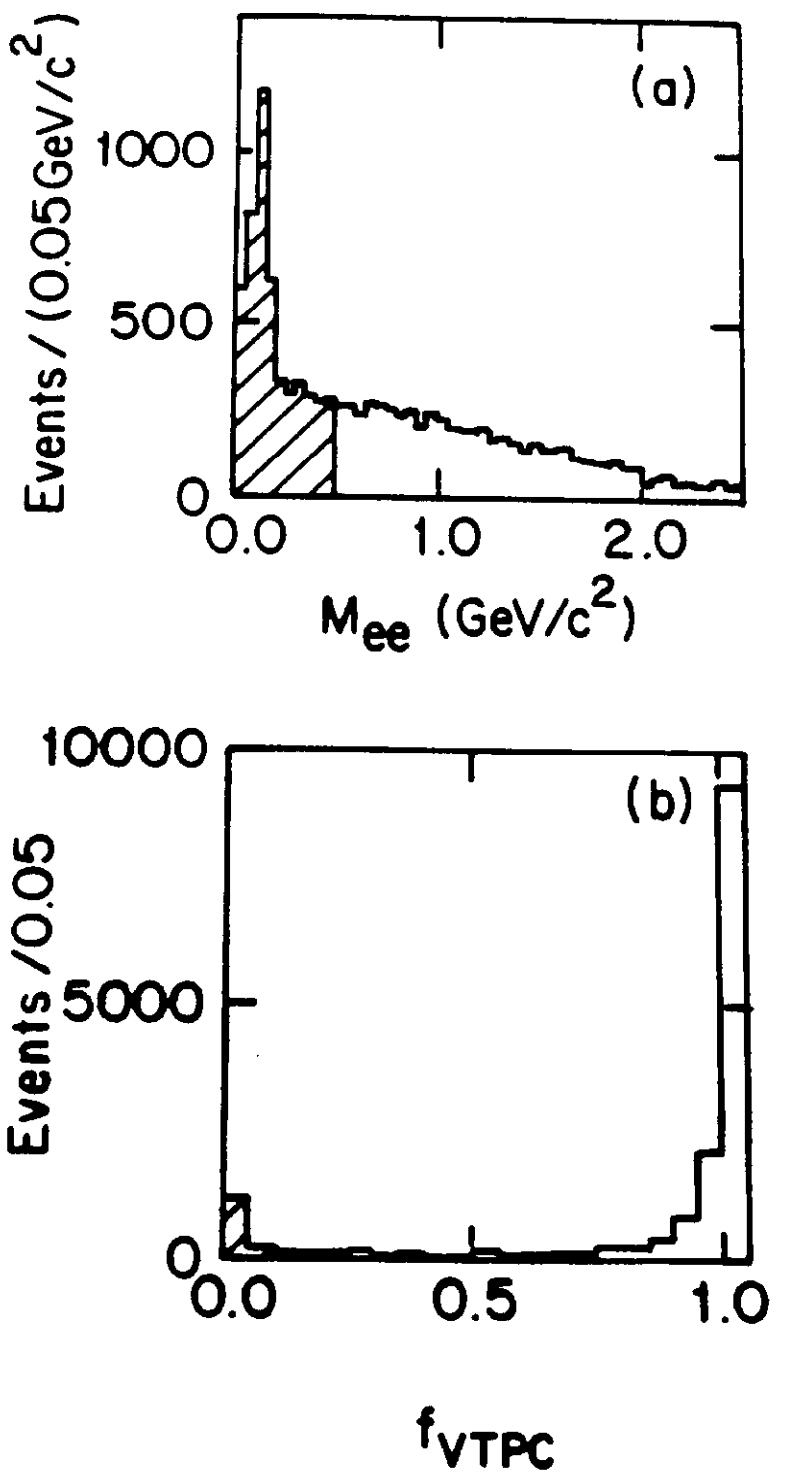

FIG. 5. The distributions for the variables used to identify conversions: (a) the invariant mass of electron candidate with a nearby track, and (b) f_{VTPC}, the fraction of expected hits observed in the VTPC along the electron's trajectory. The candidates falling in the shaded regions are rejected.

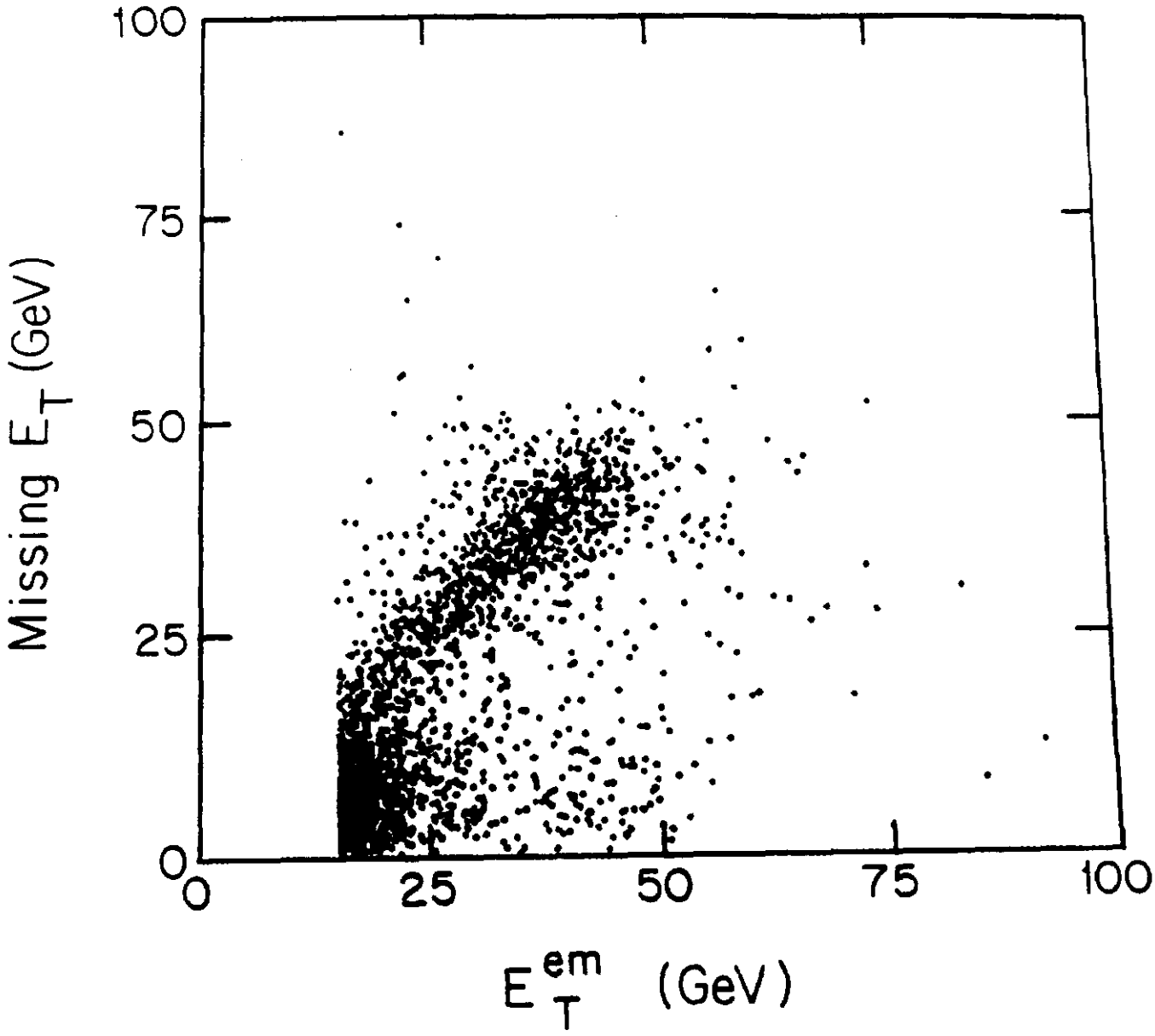

FIG. 6. Scatterplot of $\not\!\!E_T$ vs E_T^{em} for the inclusive electron sample. Only half of the total sample is shown for clarity.

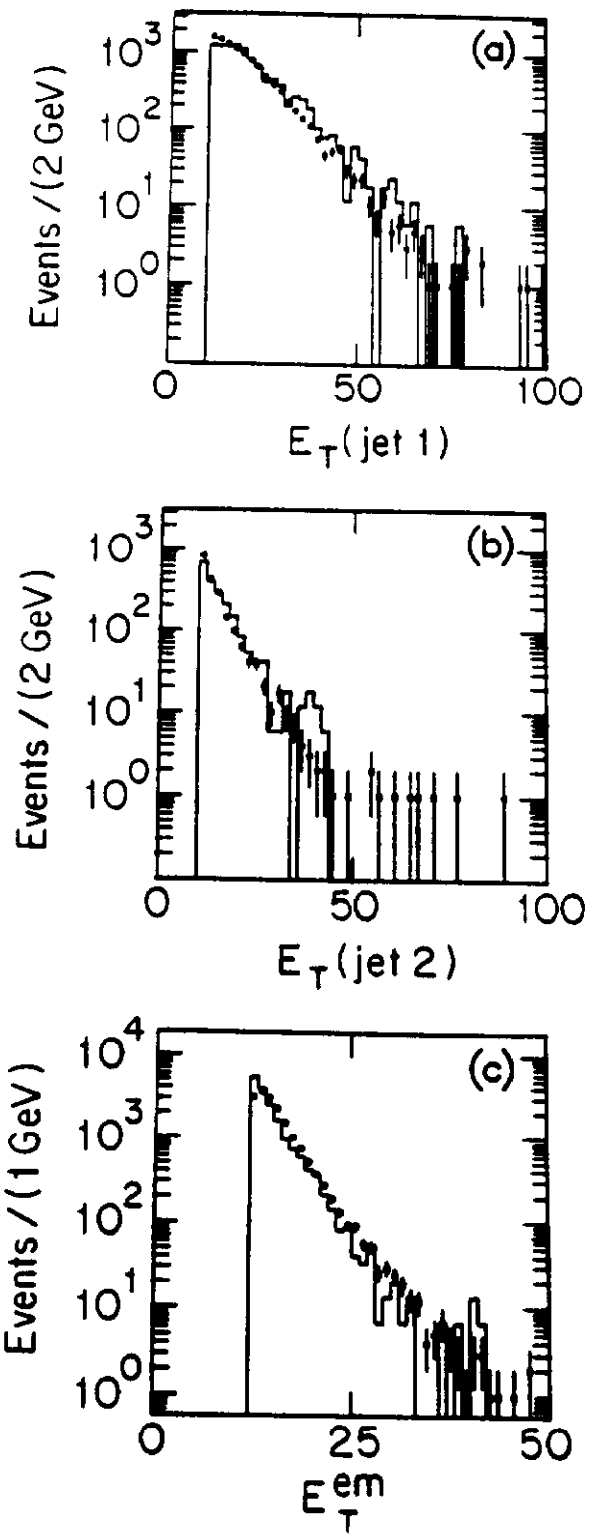

FIG. 7. The E_T distributions for the leading and non-leading jets ((a) and (b)) and for the electron candidates (c) are shown as the plotted points. The histograms are the Monte Carlo predictions for b and c quark production.

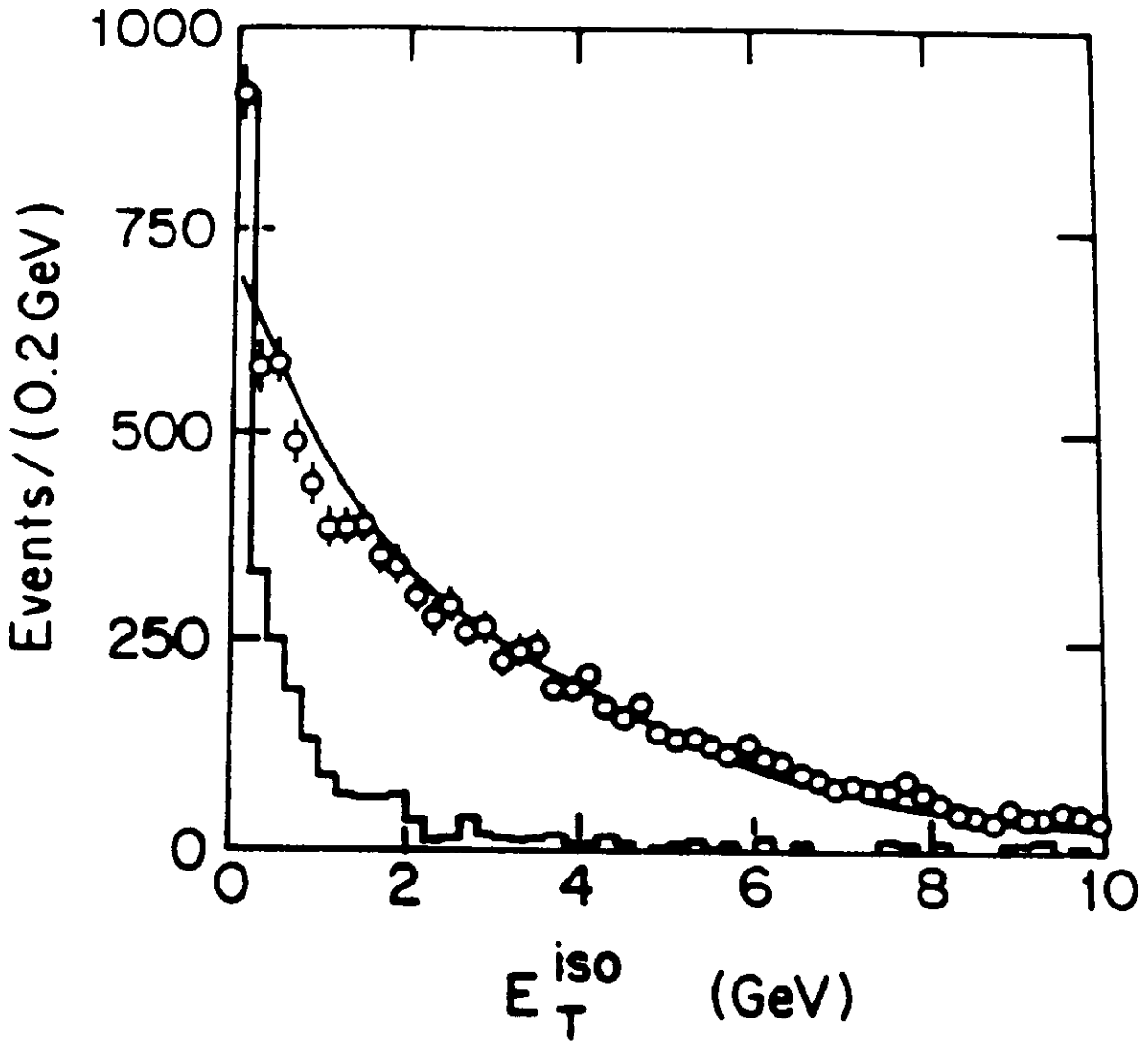

FIG. 8. Isolation variable E_T^{iso} for electrons with $E_T^{em} < 20\ GeV$, for data (plotted points), $b\bar{b}$ Monte Carlo (solid curve), and $t\bar{t}$ ($M_{top} = 75\ GeV$, histogram). Residual $W^{\pm}$ and Drell-Yan events form the peak in the very lowest E_T^{iso} bin. The normalization of the Monte Carlo curves is discussed in the text.

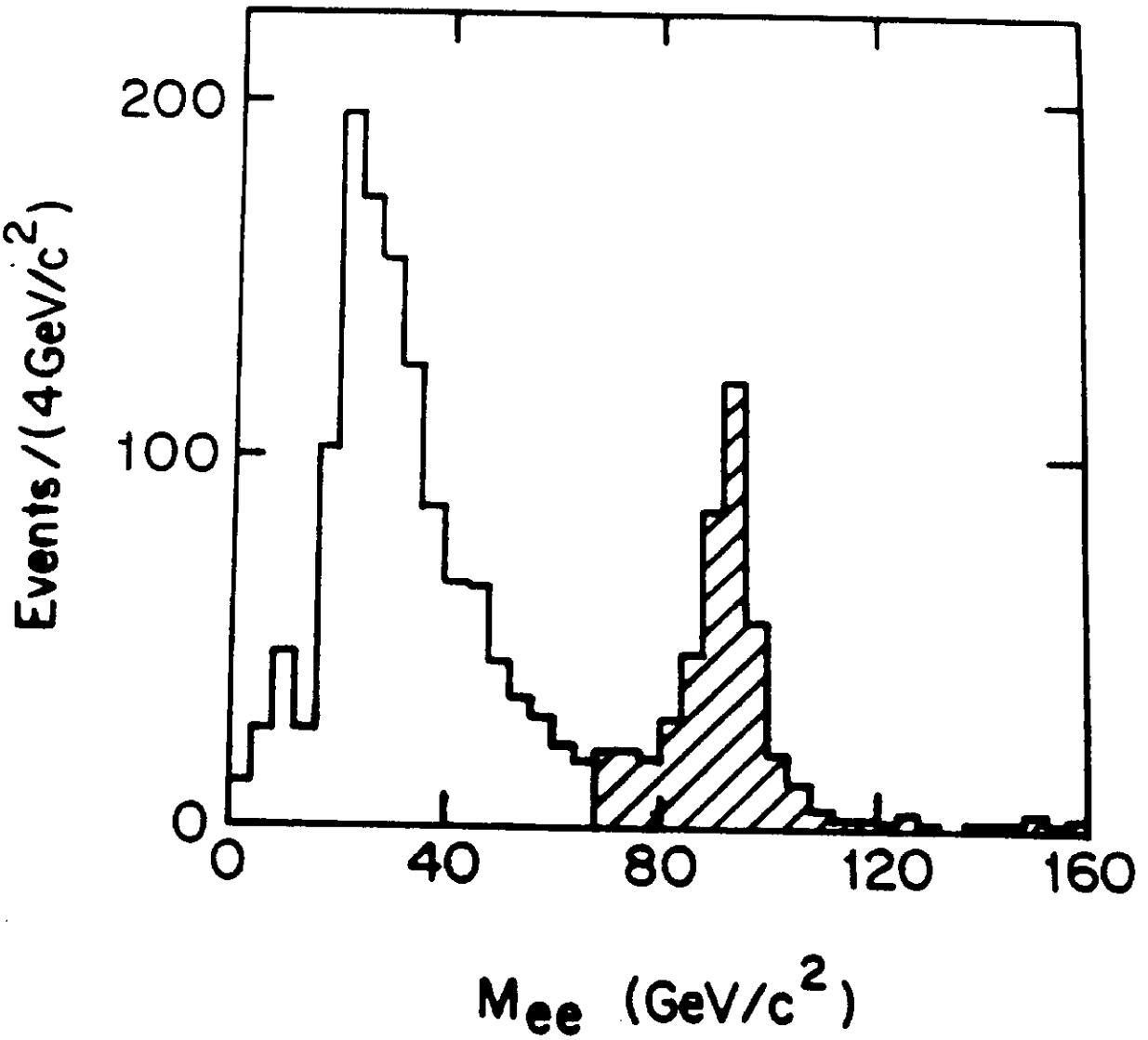

FIG. 9. Mass spectrum of di-electron candidates. The shaded region is cut.

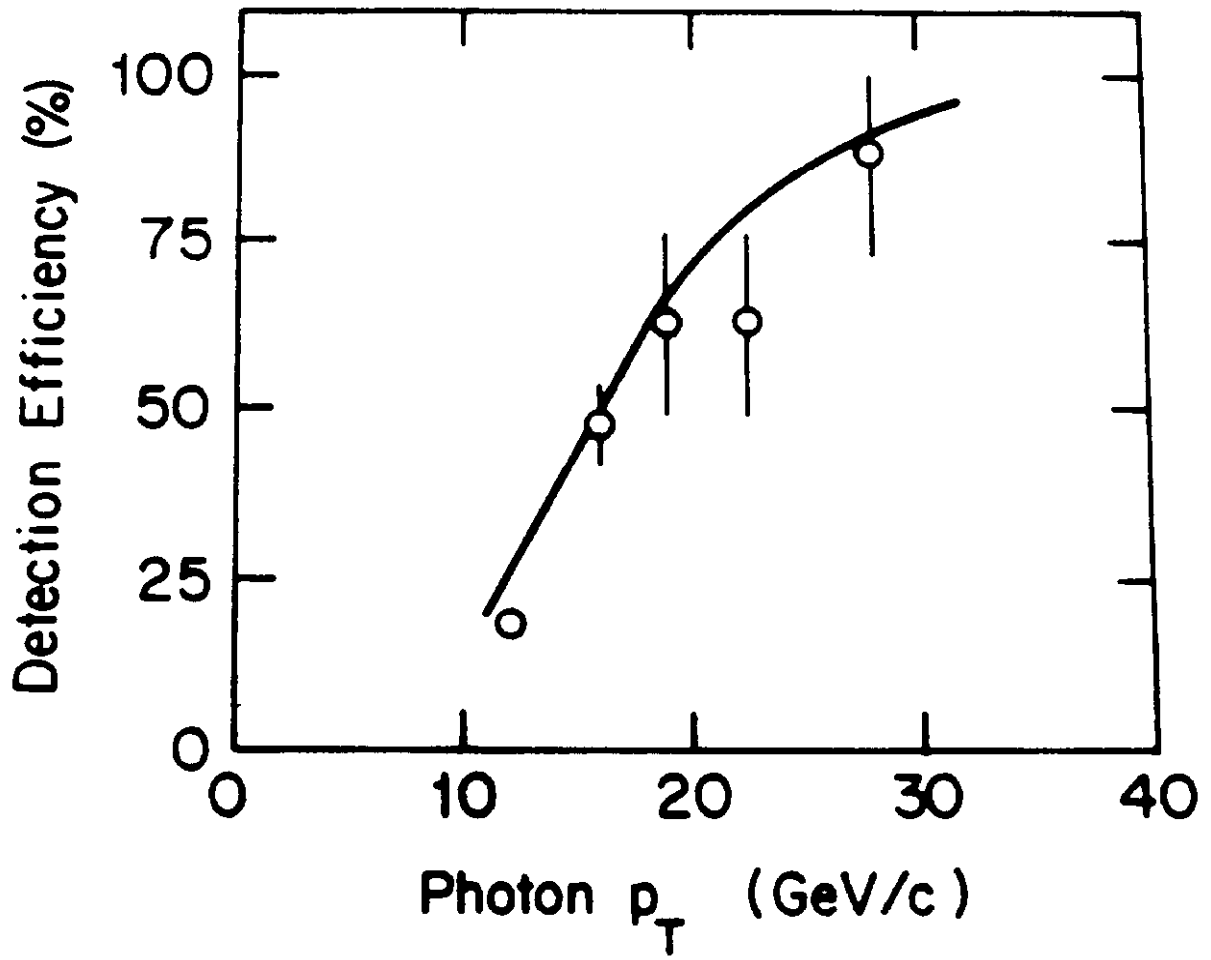

FIG. 10. Probability of finding a jet cluster with observed $E_T > 10$ GeV in the hemisphere opposite the photon for direct photon events. The horizontal axis is the photon p_T (assumed equal to the parton p_T). The solid curve is the Monte Carlo prediction.

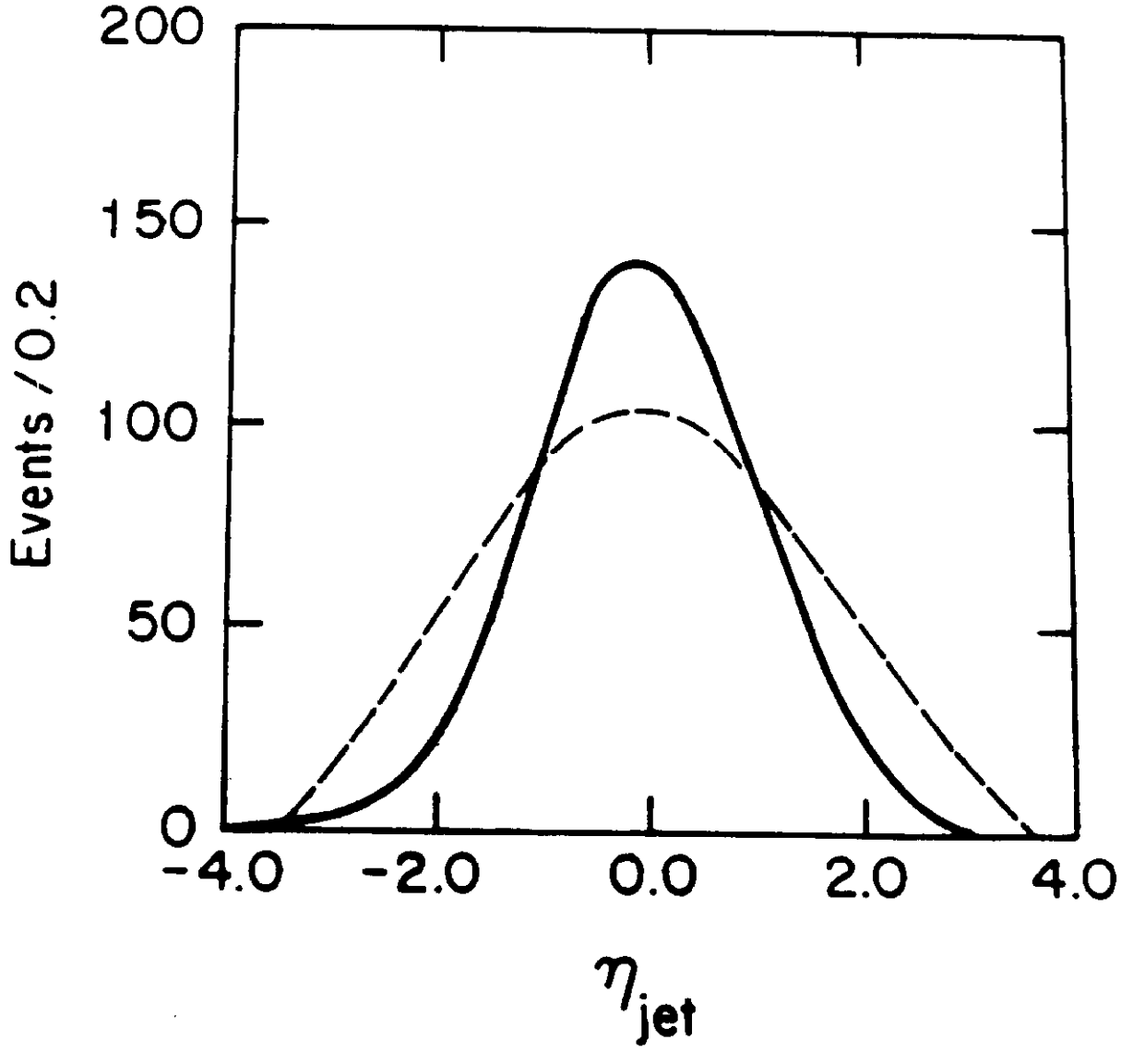

FIG. 11. Monte Carlo distributions of the pseudorapidity of jets from top (M_{top} = 75 GeV/c^2, solid curve) and W + 2 jet events (dashed curve).

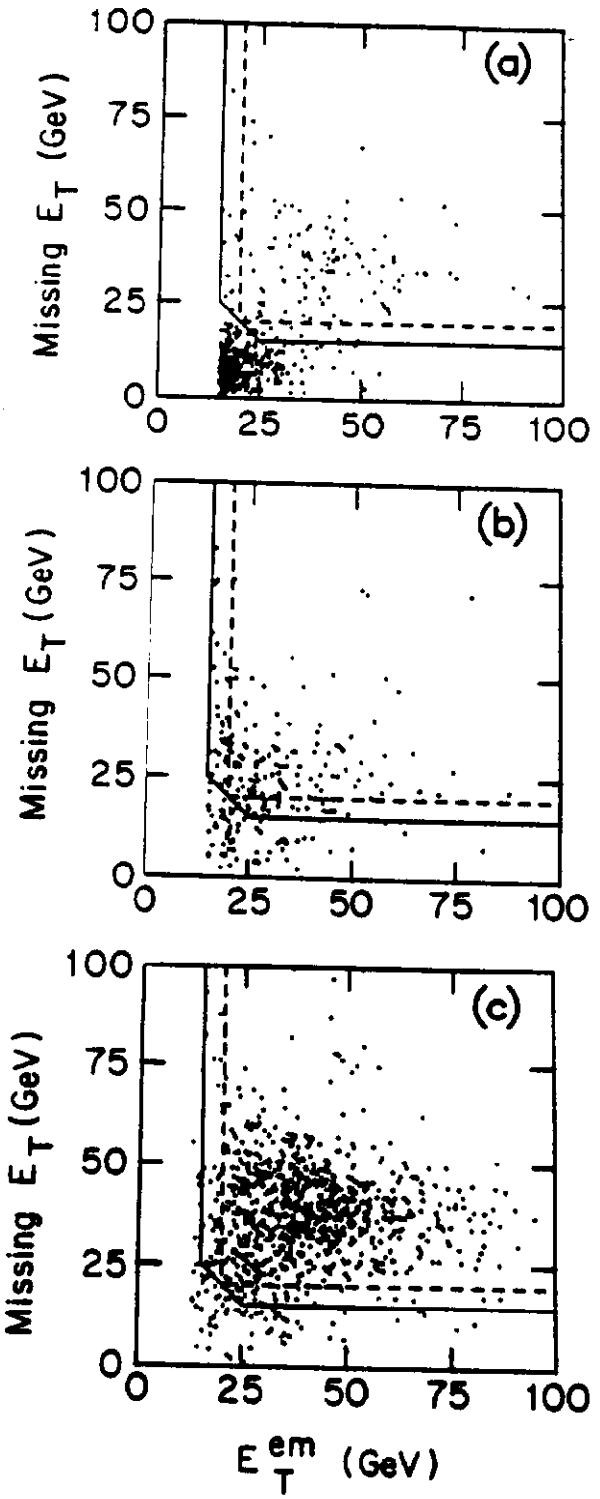

FIG. 12. Scatterplot of $\not\!\!E_T$ vs E_T^{em} for events with an electron and two or more jets. Conversions and Z^0 events have been removed as described in the text. The plot for the data events is shown in (a) along with the contours for the tight and loose kinematic cuts. Plot (b) shows Monte Carlo $t\bar{t}$ events with M_{top} = 70 GeV/c^2, and plot (c) shows Monte Carlo W + 2 jet events. The integrated luminosities of the $t\bar{t}$ and W + jet samples are 13 pb^{-1} and 41 pb^{-1}, respectively.

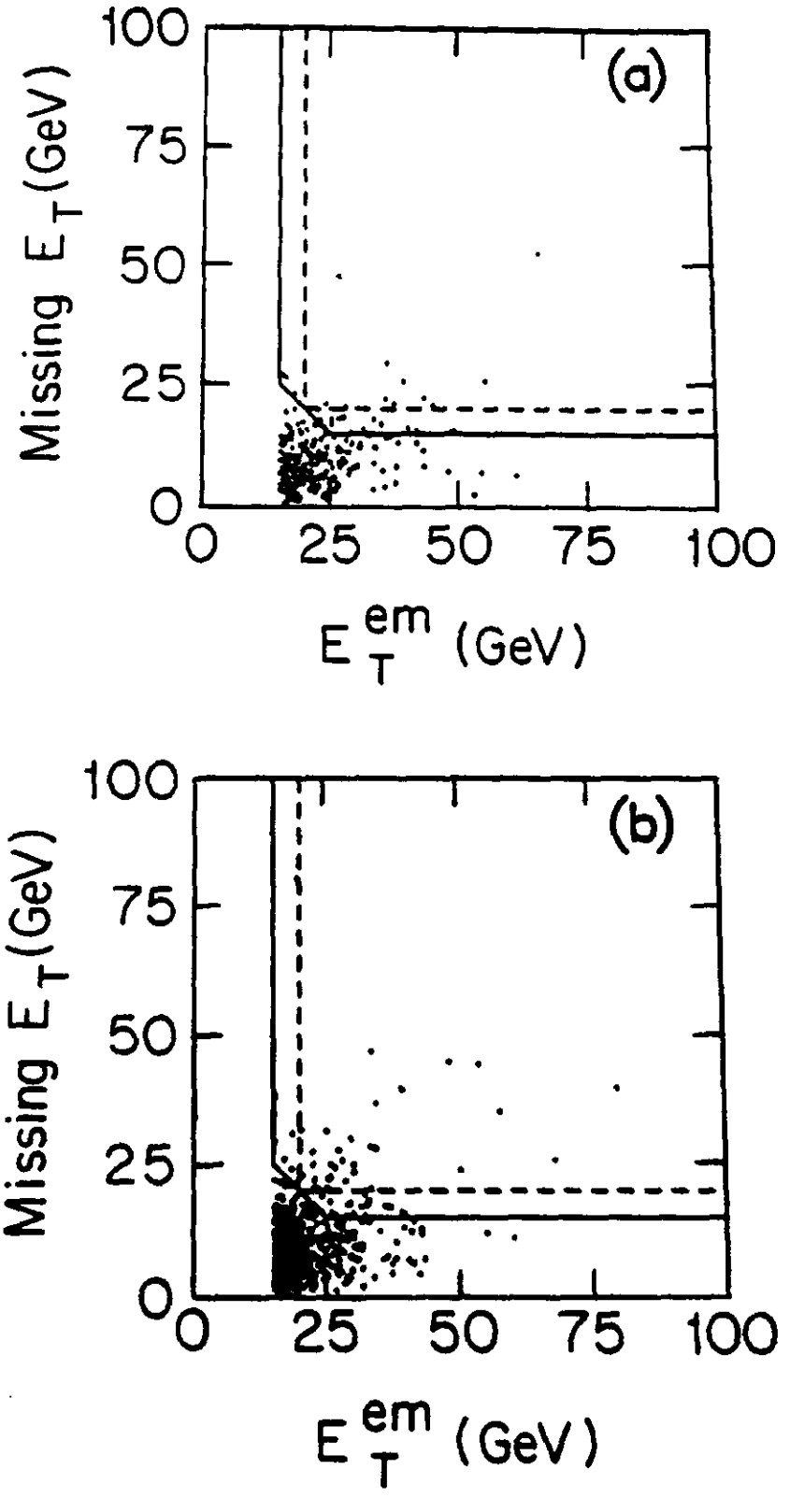

FIG. 13. The $\not\!\!E_T$ vs E_T^{em} scatterplot for background events: (a) shows the distribution for conversion events and (b) shows it for non-isolated electrons ($E_T^{iso} > 2$ GeV).

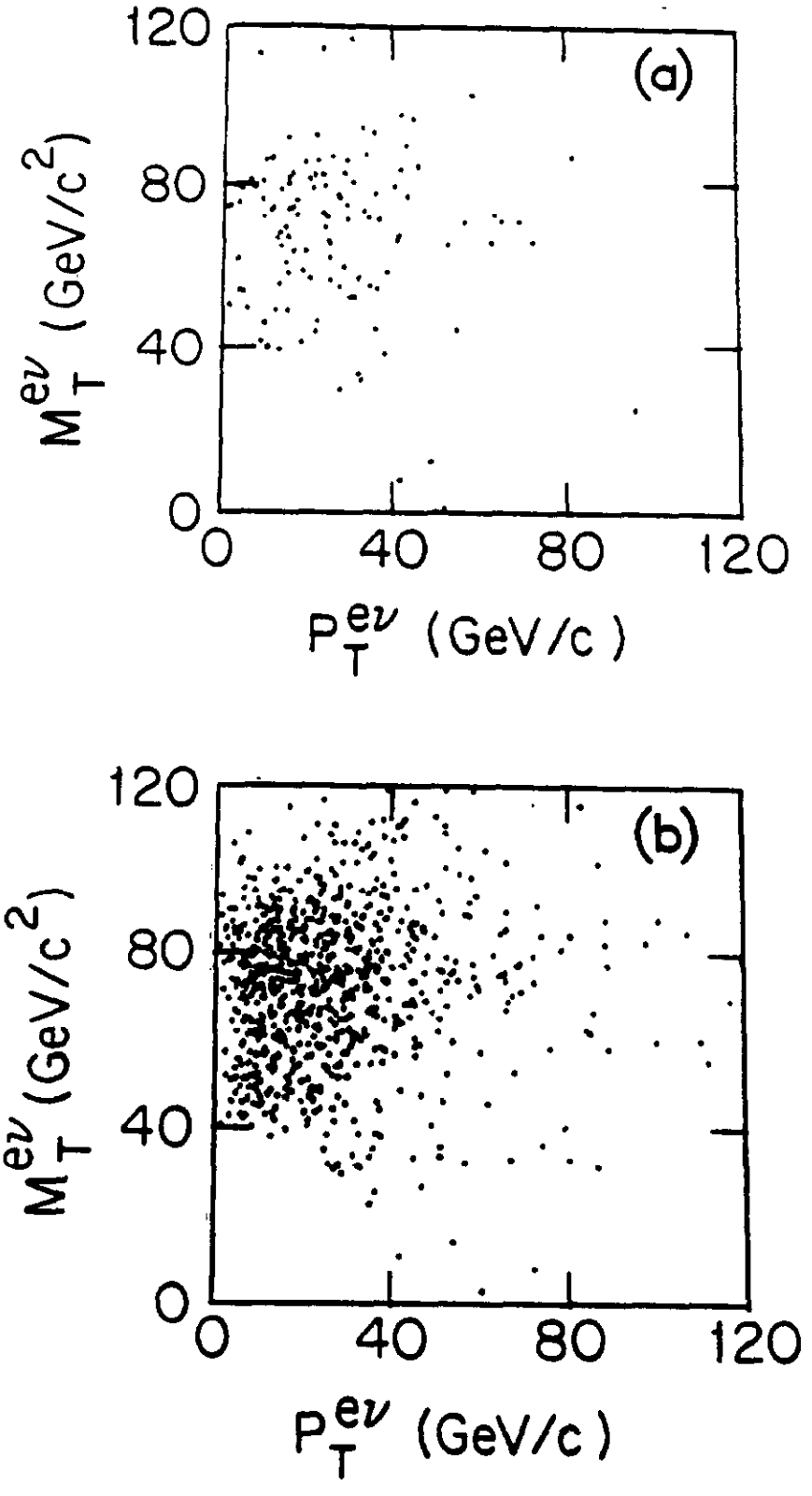

FIG. 14. The scatterplot of $M_T^{e\nu}$ vs $p_T^{e\nu}$ for the electron + 2 jet data sample with the loose cuts is shown in (a). For comparison, we show the corresponding distribution for the W + 2 jet Monte Carlo events in (b).

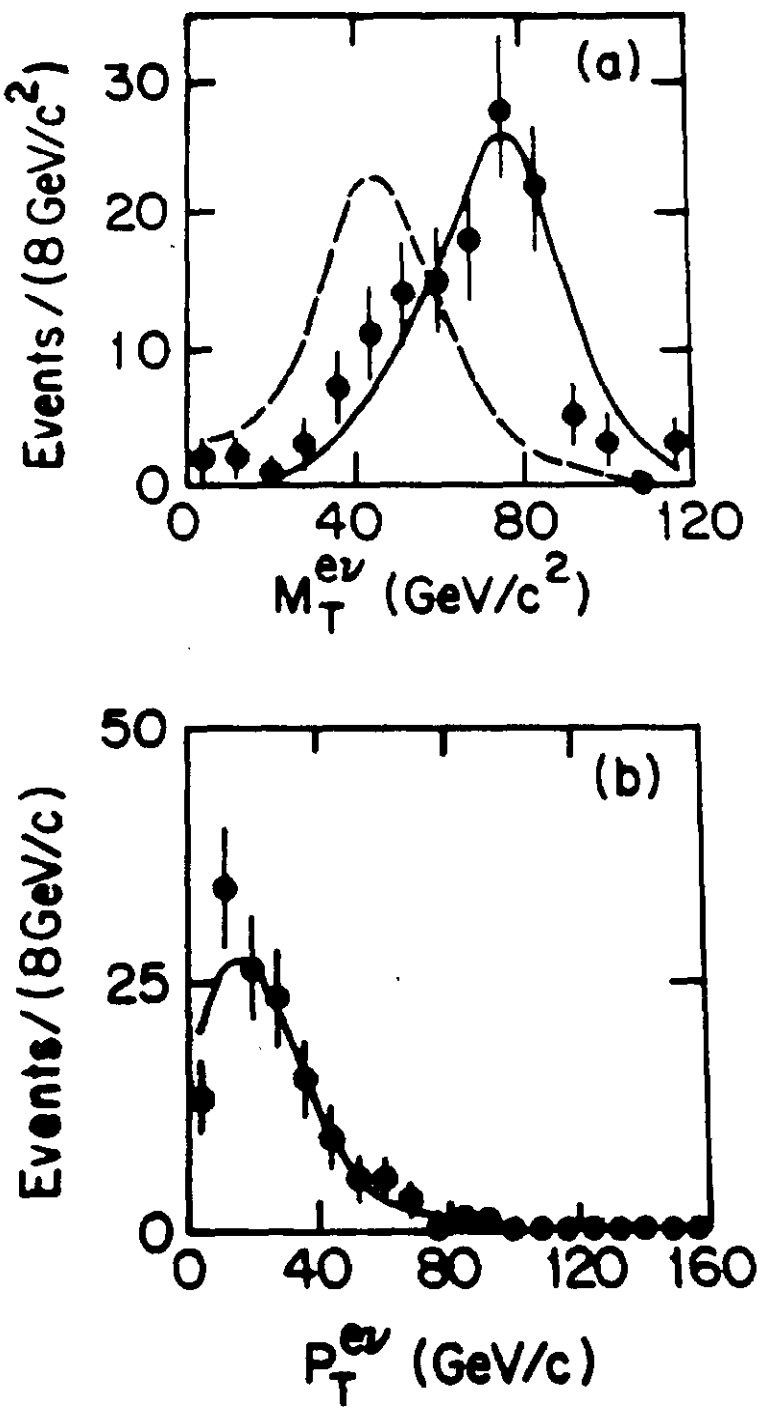

FIG. 15. The $M_T^{e\nu}$ and $p_T^{e\nu}$ distributions for electron + 2 jet data with the loose cuts applied is shown in (a) and (b). The solid curves show the distributions for the Monte Carlo W + 2 jet events (normalized to the data), and the dashed curve shows the distributions for Monte Carlo $t\bar{t}$ events for M_{top} = 60 GeV/c² (normalized to the number of events predicted by the Altarelli cross section).

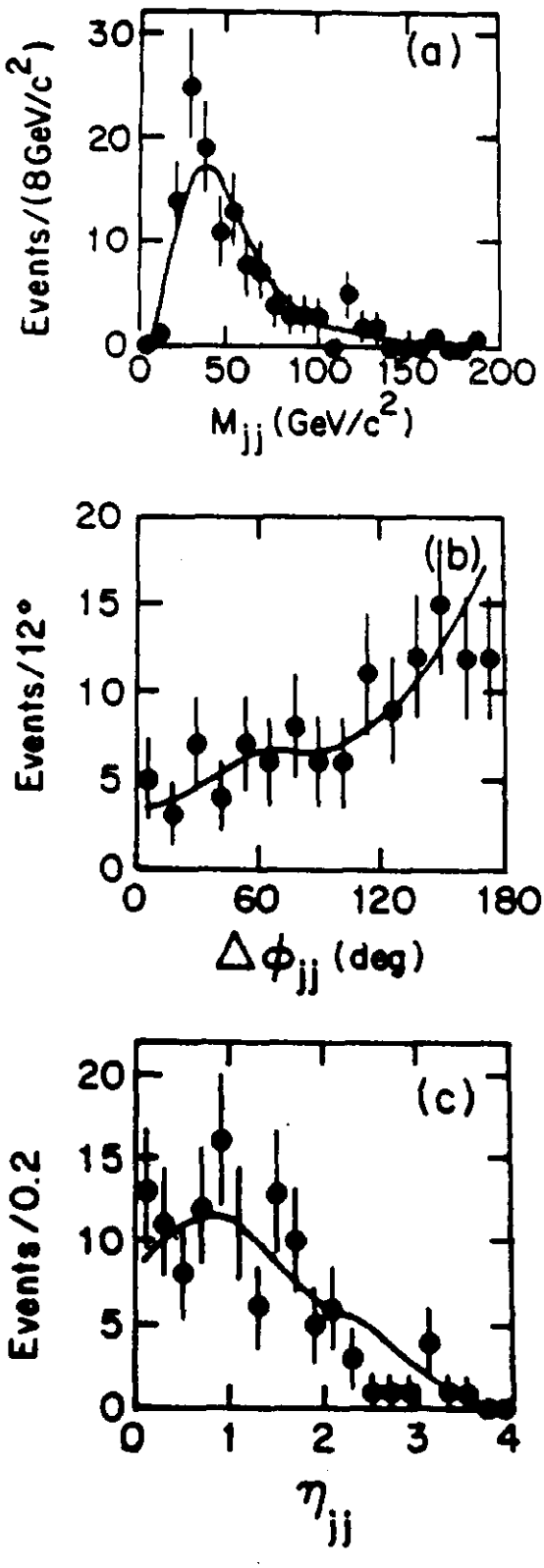

FIG. 16. Comparison of the electron + 2 jet data with the loose cuts applied (plotted points) with the W + 2 jet Monte Carlo predictions (solid curves): plot (a) shows the di-jet invariant mass distribution, plot (b) shows the distribution of the azimuthal difference between the two leading jets, and plot (c) shows the distribution of the pseudorapidity difference between the two leading jets.

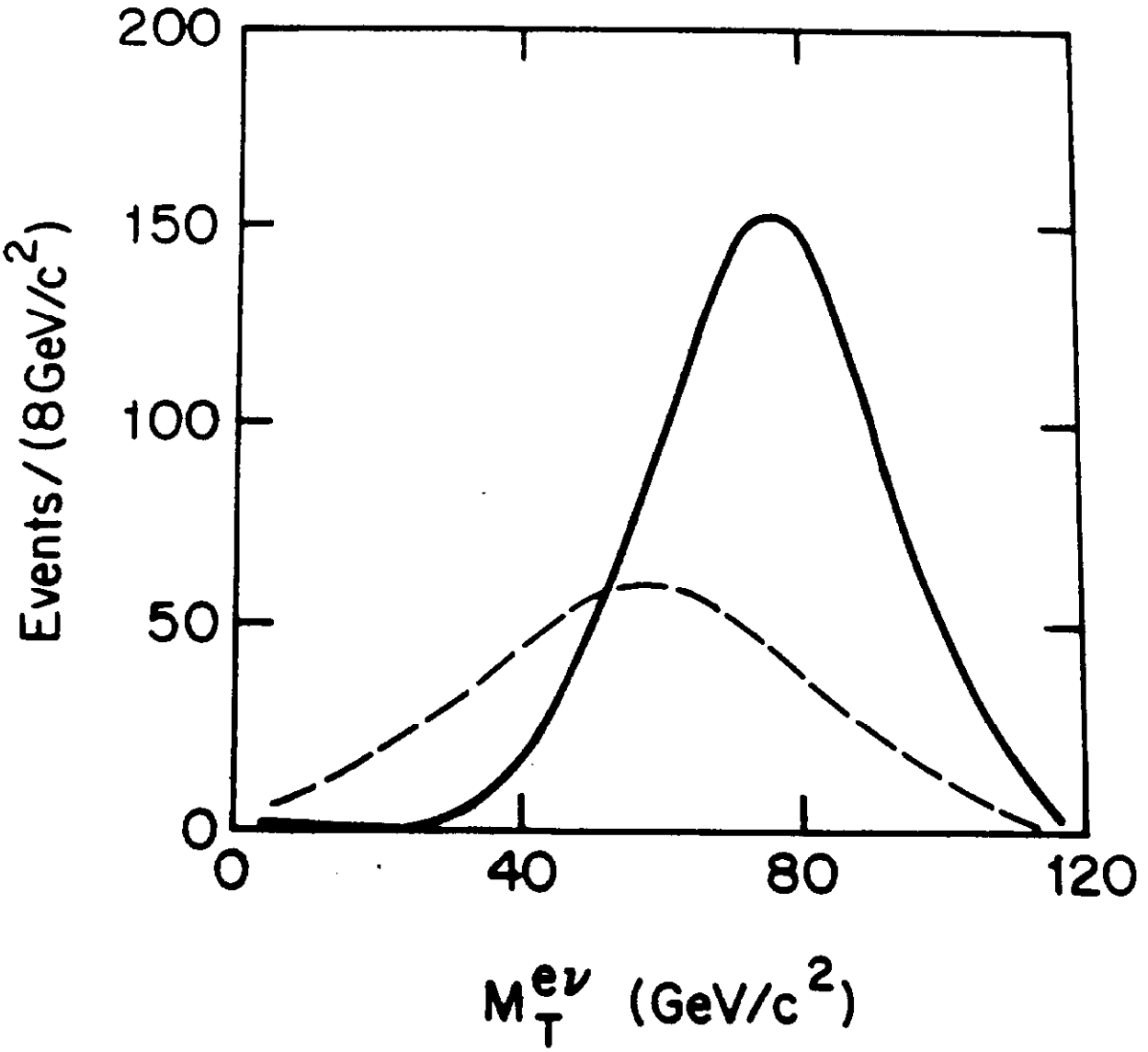

FIG. 17. Monte Carlo distributions of $M_T^{e\nu}$ for top quarks with M_{top} = 75 GeV/c^2 (dashed curve) and W + 2 jet events (solid curve).

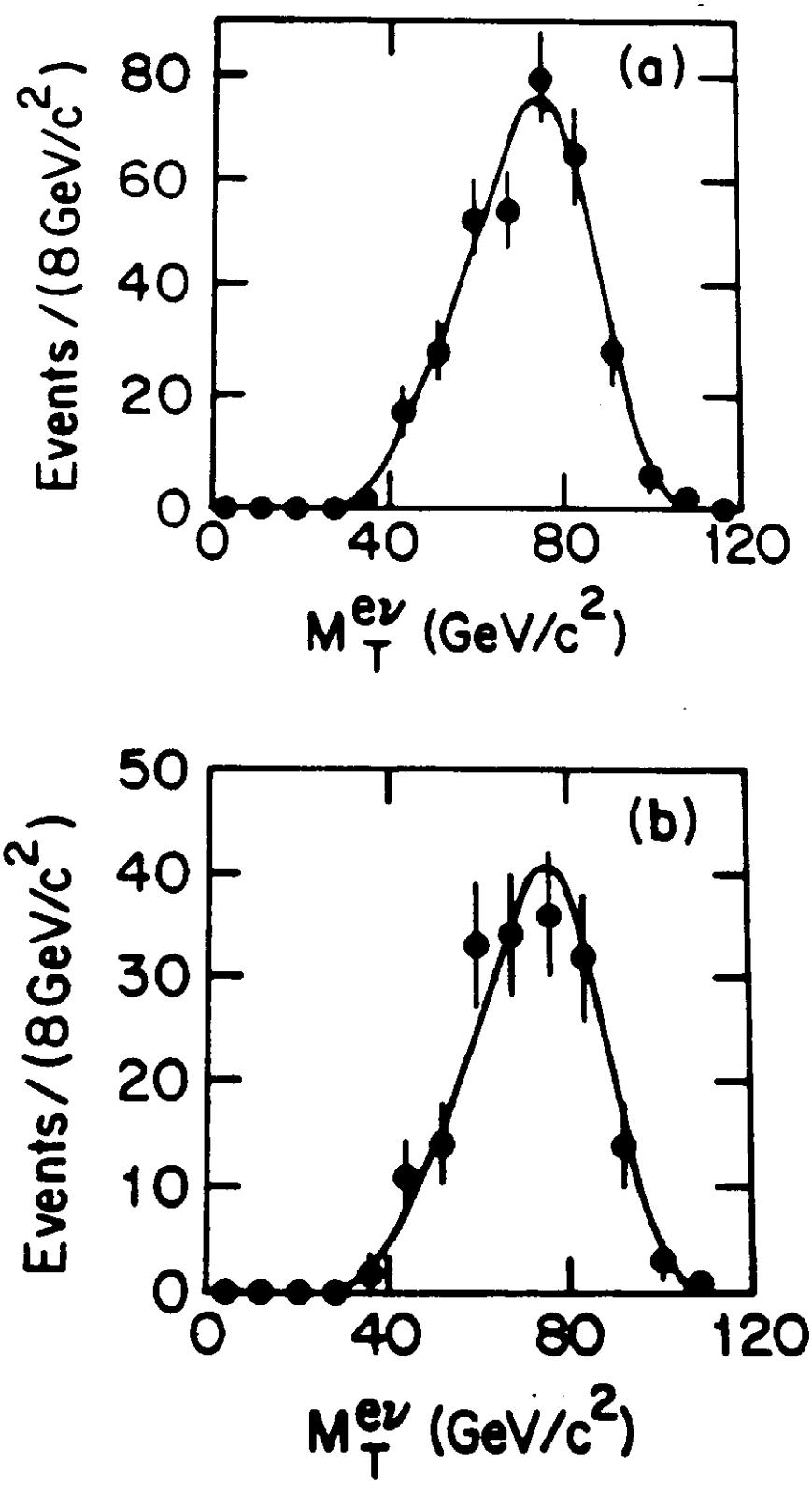

FIG. 18. Transverse mass distribution for electron + 1 jet events with the tight cuts applied. The full electron + 1 jet sample is shown in (a), and a subset of electron + 1 jet events where more $M_T^{e\nu}$ smearing is expected (as described in the text) is shown in (b).

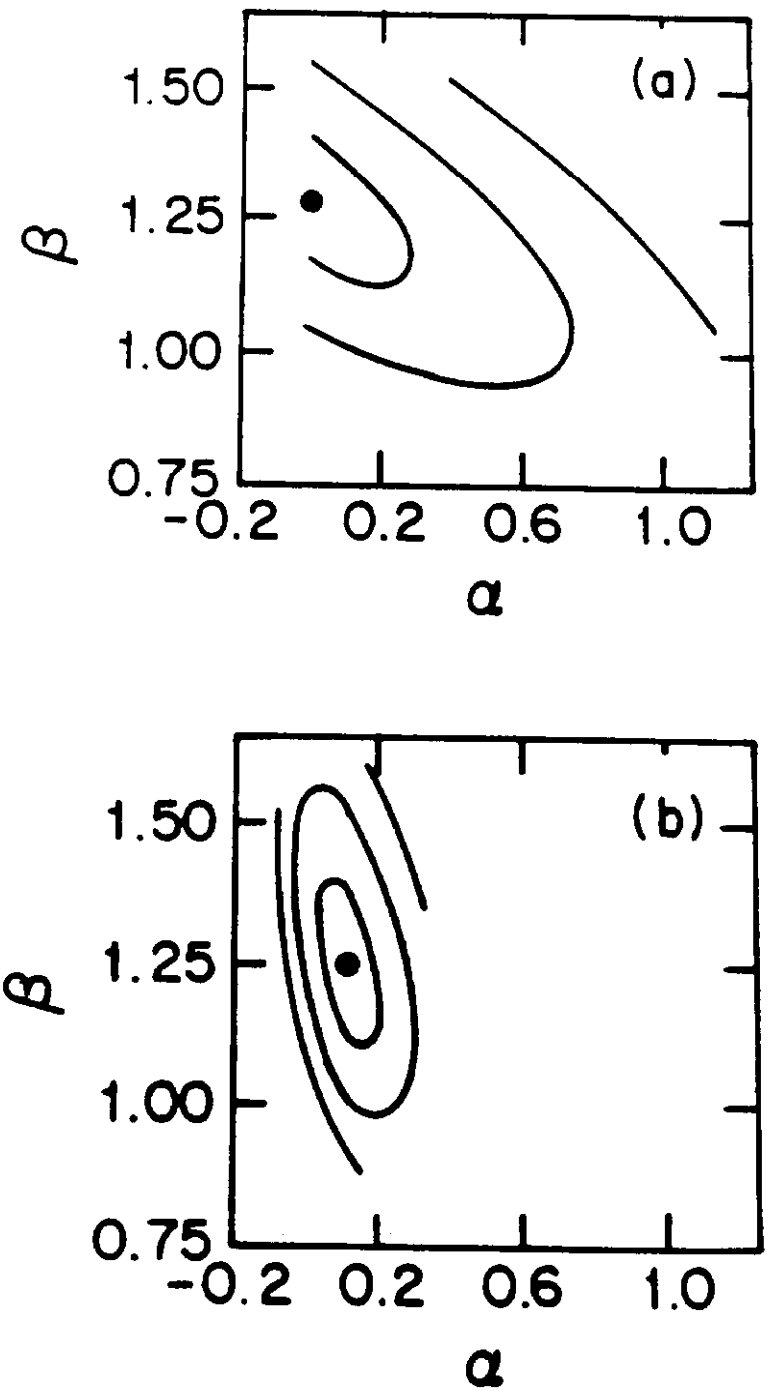

FIG. 19. Fit contours in α–β space, as calculated by MINUIT. The contour for the fit to M_{top} = 80 GeV/c^2 is shown in (a), and for M_{top} = 60 GeV/c^2 in (b). The contours correspond to changes in the log-likelihood function of 0.5, 2.0, and 4.5. The constraint $\alpha > 0$ has been imposed for the 80 GeV/c^2 fit.

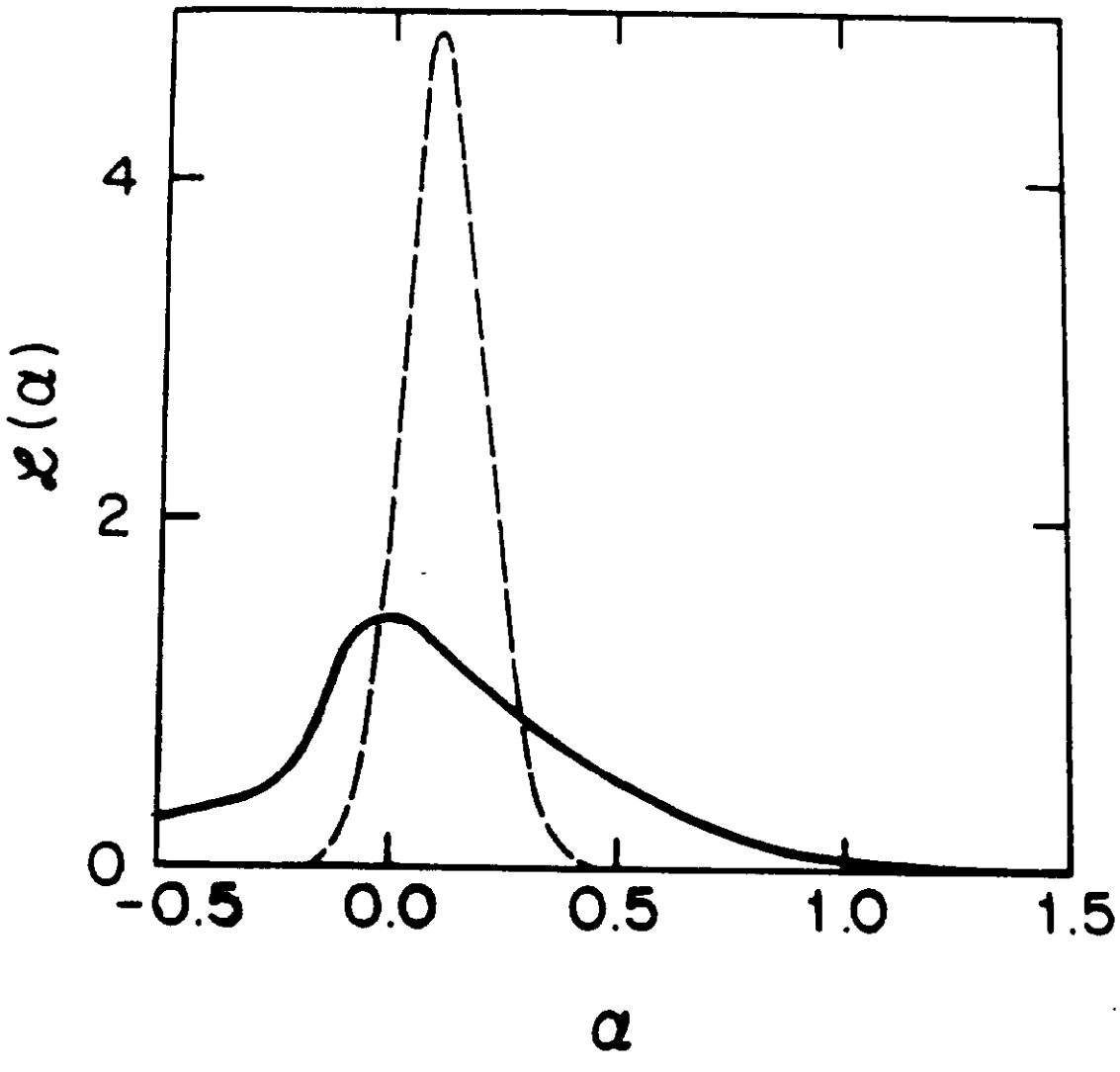

FIG. 20. Normalized likelihood distributions for the 80 (solid curve) and 60 (dashed curve) GeV/c^2 fits.

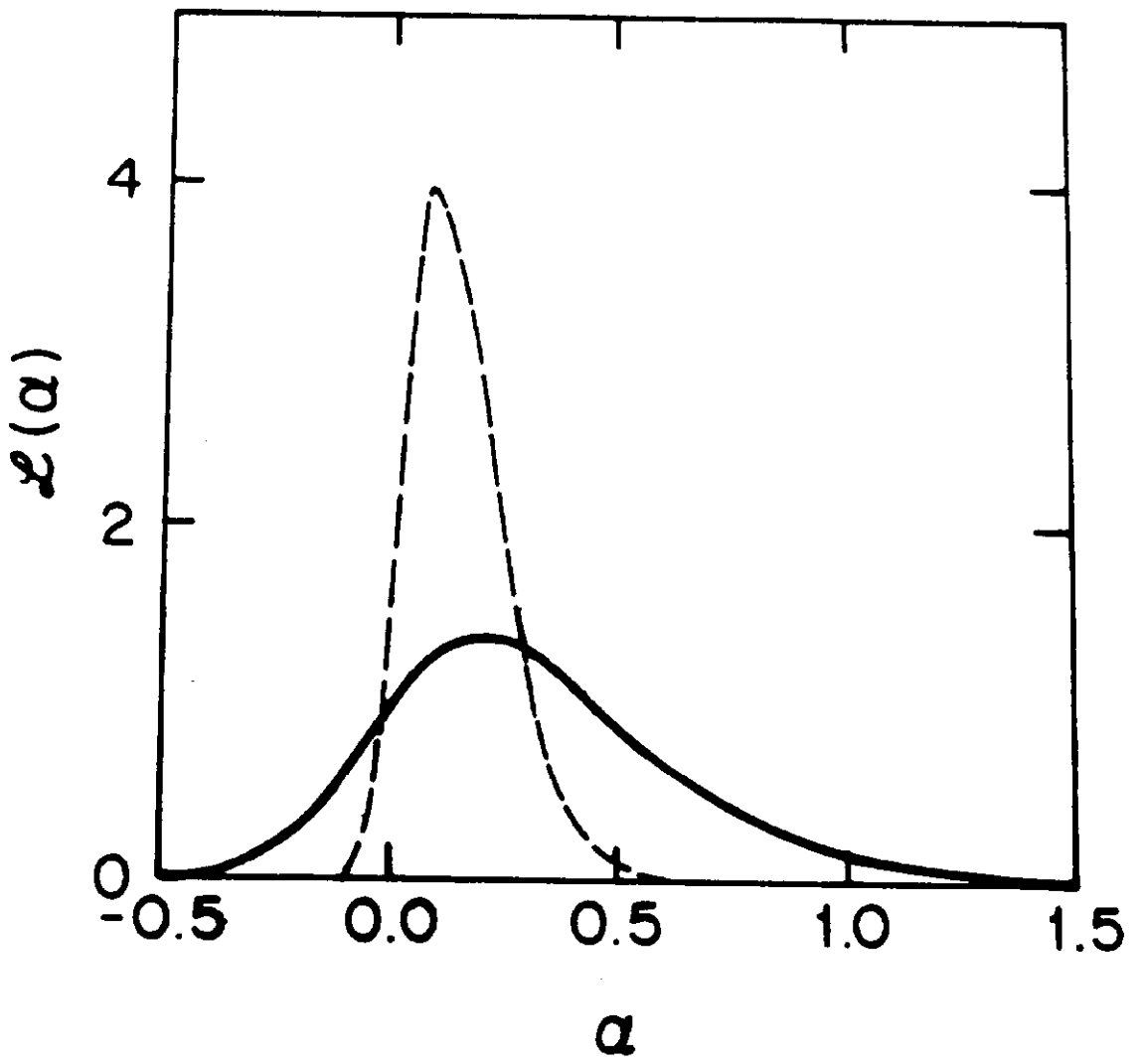

FIG. 21. Smeared likelihood distributions for the 80 (solid curve) and 60 (dashed curve) GeV/c^2 fits.

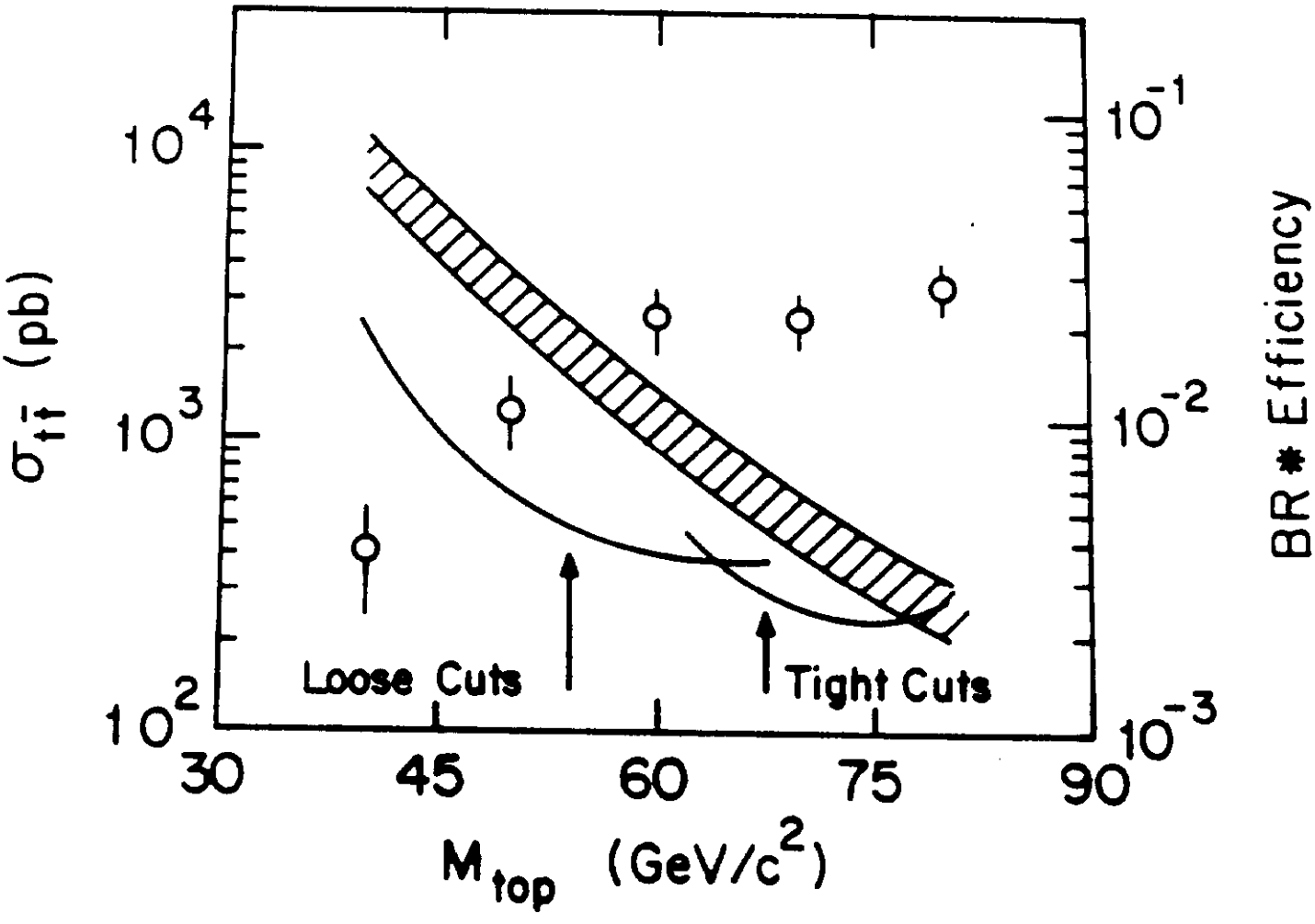

FIG. 22. The 95% C.L. upper limit for the $t\bar{t}$ production cross section as a function of top mass is given by the solid curves. The shaded region gives the predicted $t\bar{t}$ cross section (see text). The plotted points show the $t\bar{t}$ efficiency as a function of M_{top} (right-hand scale).

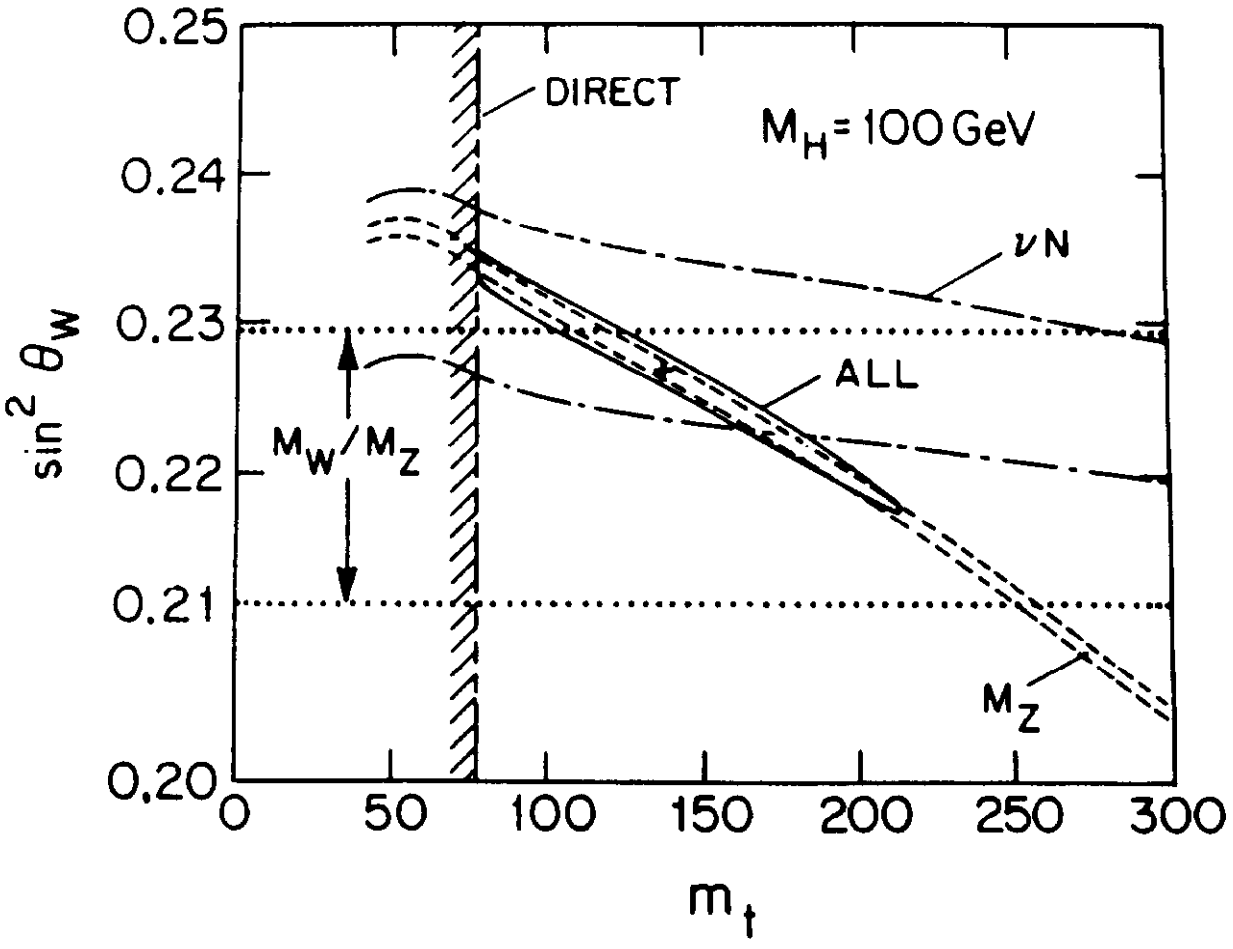

FIG. 23. The $\pm 1\sigma$ uncertainties in $\sin^2\theta_W \equiv 1 - M_W^2/M_Z^2$, determined from M_Z (dashed line), M_W/M_Z (dotted line), and νN neutral current data (dash-dotted line) as a function of M_{top} for $M_H = 100$ GeV/c^2. Also shown is the direct lower limit from the nonobservation of the t quark in $\bar{p}p \to t\bar{t} + X$ (long-short line), and the region (solid line) in $\sin^2\theta_W$-M_{top} allowed by all data at 90% CL ($\Delta\chi^2 = 4.6$).